DISSERTATIONS IN
FORESTRY AND
NATURAL SCIENCES

Jari Kourunen

Imaging of Mixing in Selected Industrial Processes Using Electrical Resistance Tomography

Publications of the University of Eastern Finland
Dissertations in Forestry and Natural Sciences

UNIVERSITY OF
EASTERN FINLAND

JARI KOURUNEN

Imaging of mixing in selected industrial processes using electrical resistance tomography

Publications of the University of Eastern Finland
Dissertations in Forestry and Natural Sciences
No 166

Academic Dissertation
To be presented by permission of the Faculty of Science and Forestry for public examination in the Auditorium SN200 in Snellmania Building at the University of Eastern Finland, Kuopio, on December, 13, 2014,
at 12 o'clock noon.

Department of Applied Physics

Grano Oy
Kuopio, 2014
Editor: Prof. Pertti Pasanen, Prof. Pekka Kilpelinen,
Prof. Kai Peiponen, Prof. Matti Vornanen

Distribution:
University of Eastern Finland Library / Sales of publications
P.O. Box 107, FI-80101 Joensuu, Finland
tel. +358-50-3058396 http://www.uef.fi/kirjasto

ISBN: 978-952-61-1637-2 (printed)
ISSNL: 1798-5668
ISSN: 1798-5668
ISBN: 978-952-61-1638-9 (pdf)
ISSNL: 1798-5668
ISSN: 1798-5676

Author's address:
University of Eastern Finland
Department of Applied Physics
P.O.Box 1627
FI-70211 KUOPIO
FINLAND
email: jari.kourunen@uef.fi

Supervisors:
Professor Marko Vauhkonen, Ph.D.
University of Eastern Finland
Department of Applied Physics
P.O.Box 1627
FI-70211 KUOPIO
FINLAND
email: marko.vauhkonen@uef.fi

Lasse Heikkinen, Ph.D.
University of Eastern Finland
Department of Applied Physics
P.O.Box 1627
FI-70211 KUOPIO
FINLAND
email: lasse.heikkinen@uef.fi

Reviewers:
Professor Daniel Sbárbaro, Ph.D.
Universidad de Concepción
Department of Electrical Engineering
Edmundo Larenas 219
Concepción
CHILE
email: dsbarbar@udec.cl

Manuchehr Soleimani, Ph.D.
University of Bath
Department of Electronic and Electrical Engineering
Claverton Down
BA2 7AY Bath
UNITED KINDOM
email: M.Soleimani@bath.ac.uk

Opponent:
Professor Tuomas Koiranen, Ph.D. (Tech.)
Lappeenranta University of Technology
LUT Chemtech
Faculty of Technology
P.O.Box 20
53851 LAPPEENRANTA
FINLAND
email: Tuomas.Koiranen@lut.fi

ABSTRACT

Today's process industry faces many challenges due to several factors. Examples are environmental acts and increased expectations of economical profits. For the process industry, these mean increased process efficiency for improved sustainability and competitiveness, leading to process optimization, continuous process monitoring and control of processes.

Mixing is one of the basic processes in many industrial fields. The quality of mixing greatly affects the process outputs and end products. Common features for mixing phenomena are that they are fast, mixed process materials are usually opaque, and mixing is a volumetric process.

Information on industrial mixing processes is usually based on offline laboratory tests, in situ measurements, or computational fluid dynamics (CFD). The requirements for online measurement methods of mixing processes are that they have to be non-invasive, fast enough with respect to the process time span and capable of producing information about the whole mixing volume. The first two requirements can usually be met. However, these techniques, both in laboratory and plant scales, are usually point-wise measurements; this means that they only give local information about the mixing. Therefore, there is a need for new measurement techniques which meet all three requirements.

In this thesis, the feasibility of three-dimensional Electrical Resistance Tomography (ERT) for monitoring certain selected mixing processes in the pulp and paper and mineral industries is studied. ERT is an imaging method in which alternating electrical currents and measured voltages from the boundary of the object aid in the estimation of the real valued conductivity distribution within the object.

In this study, a multifunctional, modular ERT system was developed and optimized for imaging industrial mixing processes. This system was used for monitoring the mixing of two miscible liquids in a turbulent flow using two mixing systems of papermak-

ing chemicals and additives. The system was also used to study mixing phenomena in a medium-consistency mixer in the pulp industry. Finally, this ERT technique was used to characterize the three-dimensional gas holdup distribution in a mechanical laboratory flotation cell.

The results show that the chosen mixing processes can be studied successfully with the ERT system developed. The tomographic technology developed can be used in designing and optimizing mixing devices in the mineral and pulp and paper industries.

Universal Decimal Classification: 537.31, 622.795, 658.562.44, 676.024.17, 676.026

INSPEC Thesaurus: process monitoring; mixing; paper industry; paper making; paper pulp; pulp manufacture; mineral processing industry; mineral processing; flotation (process); liquid mixtures; flow; turbulence; tomography; electrical conductivity; electric resistance; electric resistance measurement; electric impedance; electric impedance measurement; electric impedance imaging

Yleinen suomalainen asiasanasto: prosessinohjaus; prosessiteollisuus; sekoitus; seokset; paperiteollisuus; paperinvalmistus; virtaus; turbulenssi; tomografia; resistanssi; sähkönjohtavuus; impedanssitomografia

Acknowledgments

This thesis was carried out in the Department of Applied Physics at the University of Eastern Finland during the years 2005-2014.

I am very grateful to my supervisors Professor Marko Vauhkonen, PhD, and Lasse Heikkinen, PhD, for their excellent guidance and encouragement during these years. I also wish to thank Professor Jari Kaipio, PhD, who originally hired me in his excellent research group to carry out interesting research. In addition, I would also like to thank Tuomo Savolainen, PhD, for his friendship, encouragement and excellent guidance during these years.

I wish to thank the official reviewers Professor Daniel Sbarbaro, PhD, and Manuchehr Soleimani, PhD, for the assessment of the thesis.

I would like to thank the staff in the Department of Applied Physics at the University of Eastern Finland. Especially, I want to thank Mr. Aimo Tiihonen for his help, support and friendship during these years. I would like to thank my collegues and friends Antti Nissinen, PhD, and Kimmo Karhunen, PhD, for their support in mathematical problems during these years. I want to thank my co-authors Petteri Paananen, MSc (tech.), Ritva Käyhkö, LicSc (tech.), Jouni Matula, MSc (tech), Kari Peltonen, Msc (tech.), Jari Käyhkö, PhD, and Timo Niitti, MSc (tech.), who unfortunately passed away during my work on this thesis.

I want to thank my collegues in Outotec (Finland) Oy. Especially, Mr. Ari Suhonen for his encouragement during the years in Outotec. I would also thank all collegues in Numcore Ltd., for their friendship and support, I have had many unforgettable and excellent moments with you, cheers!

I thank my family and relatives for their support during my whole life. I also thank my friends for their support and frienship. Especially, Marko and Nina Nuutinen who helped me over the hard years. Finally, I want to thank for the most important persons in

my life: my beloved fiancée Tiina, daughter Sini and sons Simo and Samu.

I would like to acknowledge the Finnish Funding Agency for Technology and Innovation (TEKES), the collaborating companies in ITSPRO project and Finnish Centre of Exellence in Inverse Problems Research.

Kuopio Nov 5, 2014 *Jari Kourunen*

ABBREVIATIONS

2D	Two-dimensional
3D	Three-dimensional
AO	Analog output
AI	Analog input
CEM	Complete electrode model
CFD	Computational fluid dynamics
DAQ	Data acquisition unit
ECT	Electrical capacitance tomography
EIT	Electrical impedance tomography
ERT	Electrical resistance tomography
FEM	Finite element method
GUI	Graphical user interface
KIT4	Kuopio impedance tomography 4
LDV	Laser Doppler velocimetry
MC	Medium consistency
NI	National Instruments
PDA	Phase Doppler anemometry
PGA	Programmable gain amplifier
PIV	Particle image velocimetry
PXI	PCI eXtension for Instrumentation
RD	Relative deviation
RT	Real time
SNR	Signal-to-noise ratio
VCCS	Voltage-controlled-current source

NOTATIONS

A	Amplitude of the measured signal
α	Regularization parameter, projection coefficient vector
$\pi(\cdot)$	Probability density
e_l	lth electrode
ϵ	Approximation error
Γ	Covariance matrix
h	Height
I	Electric current
J	Jacobian matrix
L_v	Weighting matrix
L_σ	Regularization matrix
M_q	Mixing index
n	Unit normal vector
N	Number of samples
$N_e l$	Number of electrodes
Γ	Covariance matrix
Ω	Computation domain
$\partial\Omega$	Boundary of domain
phi	Phase of the measured signal
q	Measured quantity
$\mathcal{R}(\sigma)$	Resistivity matrix
$RD(h)$	Relative deviation
s	Standard deviviation of measured quantity
σ	Conductivity
$\sigma(x)$	Conductivity distribution
θ	Solution vector
$u(x)$	Potential distribution
U	Electrode potential
V	Measured voltages
V_{in}	Input voltage
V_r	Real part of measured voltage
V_q	Imaginary part of
v	Measurement noise
x	Parameter vector, position vector
z	Contact impedance

LIST OF PUBLICATIONS

This thesis consists of an overview and the following four original publications which are referred to in the text by their Roman numerals I-IV.

I J. Kourunen, T. Savolainen, A. Lehikoinen, M. Vauhkonen and L.M Heikkinen "Suitability of a PXI platform for an electrical impedance tomography system," *Measurement Science and Technology* **20,** 015503 (2009).

II J. Kourunen, R. Käyhkö, J. Matula, J. Käyhkö, M. Vauhkonen and L. M. Heikkinen, "Imaging of mixing of two miscible liquids using electrical impedance tomography and linear impedance sensor," *Flow Measurement and Instrumentation,* **19,** 391-396 (2008).

III J. Kourunen, L. M. Heikkinen, P. Paananen, K. Peltonen, J. Käyhkö and M. Vauhkonen "Electrical resistance tomography for evaluating a medium consistency mixer," *Nordic Pulp and Paper Research Journal,* **26(2),** 179-185 (2011).

IV J. Kourunen, T. Niitti and L. M. Heikkinen, "Application of three-dimensional electrical resistance tomography to characterize gas holdup distribution in laboratory flotation cell," *Minerals Engineering,* **24,** 1677-1686 (2011).

AUTHOR'S CONTRIBUTION

The four publications are the result of joint work with the supervisors and co-authors. Publication **I** was principally written by the author in co-operation with Tuomo Savolainen, PhD. Publications **II** and **IV** were principally written by the author, the supervisors and co-authors. Publication **III** was mainly written by the author and Lasse M. Heikkinen, PhD.

All the experiments in publications **II** and **III** done in Savonlinna FiberLaboratory at Lappeenranta University of Tehnology were designed by the author, supervisors and co-authors, Petteri Paananen, MSc (tech.), Ritva Käyhkö, LicSc (tech.) and Kari Peltonen, MSc (tech.). The experiments in publication **I** were designed by the author and Tuomo Savolainen, PhD. The experiments in publication **IV** were designed by the author, the supervisors and Timo Niitti, MSc (tech.).

The implementation and data analysis in all these publications were done by the author. All EIT codes used in image reconstruction and data analysis were developed by the inverse problem group at the Department of Applied Physics. All the measurements in all the publications were carried out by the author. In publication **I**, the programming of the KIT4 system was done by the author using National Instruments LabView and C/C++ programming languages.

Contents

1 Introduction

Today's process industry faces many challenges posed by, for example, environmental acts and increased expectations of economical profits. For the process industry, these mean increased process efficiency for improved sustainability and competitiveness, leading to process optimization, continuous process monitoring and control of processes.

Mixing is one of the basic processes in many industrial fields. The quality of mixing greatly affects the process outputs and end products, making understanding of mixing a very crucial issue [1–3]. There are several mixing phenomena which are not yet very well known. Mixing phenomena are commonly fast, mixed process materials are usually opaque, and mixing is a volumetric process.

Information on industrial mixing processes is usually based on laboratory tests, in situ measurements, or computational fluid dynamics (CFD) [2]. The requirements for measurement methods are that they have to be non-invasive, fast enough with respect to the process time span and capable of producing information about the whole mixing volume [4–7]. The first two requirements are usually met. However, many measurement methods both in laboratory and plant scales are point-wise measurements, which means that they only give local information about the mixing [8–14]. In this thesis, the feasibility of the three-dimensional electrical tomography method for the monitoring of volumetric mixing processes in the pulp and paper and mineral industries is studied.

Electrical Impedance Tomography (EIT) is an imaging method in which, with the aid of alternating electrical currents and measured voltages from the boundary of the object, the complex valued conductivity, i.e., admittivity distribution within the object, is estimated [15–18]. It is common that instead of the admittivity distribution, the real valued conductivity distribution is estimated. In this case, the method is called Electrical Resistance Tomography

(ERT); this thesis uses this method.

Imaging of mixing processes with the ERT approach is based on the assumption that the ingredients of the process substance have different conductivities. Fortunately, this is true in many mixing applications. If this is not the case, it is also possible to use various tracers to study the mixing process with ERT. A tracer has to have a different conductivity compared to the surrounding material.

Mathematically speaking, the conductivity distribution estimation (image reconstruction) in ERT is a nonlinear, ill-posed inverse problem [7,19]. In such a problem, small errors in the data can produce large errors in the estimation of the conductivity distribution. Moreover, the solution of the problem is not necessarily unique [7]. There are several methods to solve the ERT image reconstruction problem, such as the backprojection algorithm [20] and the sensitivity of coefficient method [21]. In this thesis, the statistical inversion method based on Bayesian probability theory is used [22].

The past two decades have witnessed active development of image reconstruction methods. At the same time, the computational capacity of computers has dramatically increased. These developments have helped the implementation of ERT for real applications, both in the medical and industrial fields [4, 23–25]. In the medical field, ERT has been used, for example, in the monitoring of lung ventilation and the brain as well as in breast cancer detection [18, 19, 26–28]. Also, in the pharmaceutical industry and industry in general, there exist several applications in which ERT can be utilized [23–25, 29–48]. In addition, ERT has been used in geophysics, for example, in monitoring subsurface water distribution [49,50].

Apart from ERT image reconstruction, the role of the ERT measurement system is important; hence, the ongoing development of ERT measurement systems. There are many ERT systems around the world that have been designed for specific applications and purposes, both in the medical and industrial fields. ERT systems can roughly be divided into two categories, semi-paraller [51–54] and paraller [55–57]. The measurements can also be performed either in

two dimensions (2D) or three dimensions (3D). In the 2D case the measurements are performed on a 2D plane and 2D reconstructions are utilized [54,58–60]. The measurements performed in 3D can be used to estimate 3D conductivity distributions.

In many cases, EIT systems are designed and produced one item at a time, which means that the development time of the system is long and expensive [61]. In the late 1990s, National Instruments introduced the PXI platform (PCI eXtension for Instrumentation) for virtual instrumentation. In virtual instrumentation, the user can vary the functionality of the system with the software [62]. It has been shown that the PXI platform is suitable and reliable for incorporation into an electrical capacitance tomography (ECT) system [61]. It has also been shown that the construction time of the ECT system has decreased because many components are commercially available. These results indicate that an EIT system constructed using mainly PXI platform components can be developed.

Aims of the thesis

In this thesis, the main aim was to develop and study ERT in the imaging of mixing in certain selected mixing processes. More detailed aims of the thesis are summarized as follows:

1. In the first study (Publication I), the aim was to examine the performance of multifunctional, modular and effective ERT systems based mainly on commercially available components. The system developed was used in the applications studied in the last part of the thesis.

2. In the second study (Publication II), the aim was to apply ERT to the monitoring of the mixing of two miscible liquids in a turbulent flow using two mixing systems of papermaking chemicals and additives.

3. In the third study (Publication III), the aim was to investigate mixing phenomena in a medium-consistency mixer in the pulp industry with the aid of ERT.

4. In the fourth study (Publication IV), the aim was to characterize three-dimensional gas holdup distribution in a mechanical laboratory flotation cell.

The structure of this thesis is as follows. Chapter 2 reviews the processes studied. A short introduction to different electrical impedance tomography systems, measurement protocols and image reconstruction is given in Chapter 3. Chapter 4 reviews the results of the studies. Chapter 5 is a summary and conclusion section.

2 Mixing in the process industry

This chapter introduces an important subprocess, mixing, used in many industrial processes. It concentrates on mixing processes in the pulp and paper and mineral industries.

Mixing is an important process in many industrial applications. Mixing is defined as follows: *"We define mixing as the reduction of inhomogeneity in order to achieve a desired process result. The inhomogeneity can be one of concentration, phase, or temperature. Secondary effects, such as mass transfer, reaction, and product properties are usually the critical objectives"* [2].

In the pulp and paper industry, mixing has a very important role in all stages of the paper-making process. Mixing is used, for example, in wet-end processing, bleaching and repulping. In pharmaceutical processes, for example in tablet manufacturing, the mixing of different drug powders homogenously is extremely important in order to assure the high quality of the end product (tablet). In the refinery processes of the petroleum industry, mixing plays an important role in the desalting process of crude oil. In the mineral industry, the mixing of reagents and gas into the slurry in the froth flotation process has an important role, affecting the efficiency of the flotation. In this thesis, gas-liquid and liquid-liquid mixing processes in two specific pulp and paper processes and in one mineral industry process are studied with the aid of ERT. In the next section, these processes are briefly reviewed.

2.1 SELECTED MIXING PROCESSES

In this section, the mixing processes studied as part of the thesis work are briefly reviewed. The three different mixing processes

are the following: 1) in the pulp and paper industry, the injection and mixing of retention aid additives before the headbox, 2) in the pulp bleaching process, the mixing of chemicals and gases and 3) in the mineral industry, the mixing of air into the slurry in the froth flotation process.

2.1.1 Mixing of wet-end additives

In the paper industry, retention aid additives are used to increase the size of fiber flocks, that is, to increase the amount of fine and filler materials in the fiber web. Good mixing of retention aid additives improves short circulation, decreases the loss of raw materials and results in more homogenous paper [63–65]. The retention aids are normally water-soluble polymers. When long chain polymers are used, the best result is obtained when they are injected to the fiber, filler and fines flow after the pressure filters, that is, before the headbox; see Figure 2.1. Since the reaction time of the retention aid is usually very short, at maximum two seconds, the effective mixing of retention aid additives to the pulp flow is very important for obtaining optimal results [63–65].

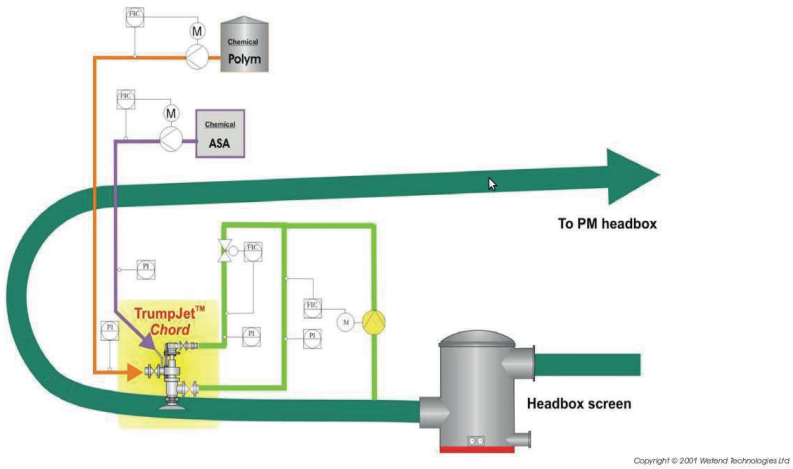

Figure 2.1: Retention aid additives injection before the headbox. The TrumpJet® jet injection system is shown in the figure (www.wetend.com).

The most common retention aid injection methods use single or multi 90 degree side entry T-pipe nozzles. These methods, however, suffer from some limitations. The injection velocity should be low to avoid the shear effect, which can destroy the efficiency of the retention aid. On the other hand, the low velocity causes ineffective mixing, which means that the retention chemical does not affect the whole volume of the pipe [64,65].

In this thesis, retention chemical mixing is studied in Paper II. The conventional and TrumpJet® injection methods were studied using the ERT technique. Saline and cold water tracers were injected to the main flow using both injection methods. The ERT system was used to monitor the mixing online and the data was analyzed for the comparison of the results of the two injection approaches.

2.1.2 Mixing in the pulp bleaching process

Pulp bleaching is an important process in paper manufacturing in which the color of the pulp is removed to make it whiter. Figure 2.2 illustrates a basic bleaching process. The pulp from the previous stage (from the digester) is washed to remove the reacted and dissolved materials which have been moved to the pulp from the process liquor. Thereafter, the pulp is heated to the reaction temperature using steam. In this stage, the pH of the pulp is set to the desired value. In the next stage, bleaching chemical(s) (Cl_2, $NaOH_2$, $MgSO_4$, O_2 and O_3) are added to the pulp suspension using a mixer. Finally, the pulp suspension is driven to a tower for a certain period of time to ensure that the chemicals have time to react with the suspension. This reaction time can vary very much depending on the chemicals used. Finally, the bleached pulp is driven to the next stage, usually through washing [2].

Chemicals are quite common in the pulp bleaching process, and these are mixed into the pulp suspension using different types of mixers [2,3]. In low-consistency (LC, pulp consistency $\leq 5\%$) conditions, the mixing of the chemicals to the pulp suspension can

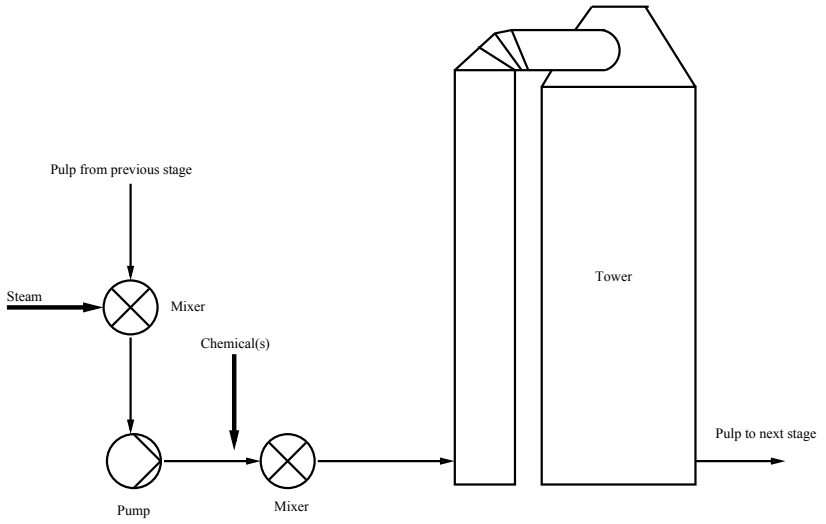

Figure 2.2: An illustration of the pulp bleaching process.

be done using continuous stirred tanks (CSTs), dynamic mixers or static mixers. In the CSTs, the mixing is done inside a vessel in which impellers mix the pulp suspension in such a way that the shear stress created by the impellers is sufficient to brake the fiber network in all the zones of the vessel. The residence time of the pulp suspension inside the vessel is important because the mixing in the CSTs produces both macro- and fiber-scale mixing, which affect how the fibers come into contact with the bleaching chemicals. Dynamic mixers are normally used in CSTs in which the pulp suspension and chemical flow are driven through a high-intensity impeller tip zone. This type of solution usually makes suspension mixing more efficient than with conventional CSTs. Static mixers are usually used in pipe sections, in which barriers are installed inside the pipe causing turbulence in the pulp suspension flow [3].

In medium-consistency (MC, pulp consistency $\geq$ 8% and $\leq$ 16%) conditions, the most commonly used mixer types are peg and high-shear. The peg mixer is a tubular vessel which has one or two shafts with pegs attached. The pulp suspension is driven through the mixer, and rotating bars shear the pulp suspension against the

stationary elements of the mixer. Chemicals can be added to the suspension ahead of the mixer or through specified injection ports located around the mixer [3]. The function of the high-shear mixers is that they attempt to fluidize the pulp suspension in the working zone. This is achieved by driving the chemicals and pulp through zones of intense shear in the mixer [2,3].

In high consistency (HC, the pulp consistency $\geq$ 20%) conditions, little or no free water is present in the pulp suspension. As an example, in one mixer solution the pulp is passed between stationary and rotating plates on which raised knobs intermesh to shear the pulp suspension [2, 3]. The chemical(s) can be added to the suspension during the mixing or inside the tower.

In this thesis, chemical mixing with an AMix AC30-25 mixer in MC conditions was studied with ERT; see Paper III. The mixing efficiency and spatial distribution of the mixing were computed and analyzed.

2.1.3 Mixing in froth flotation

In the mining industry, valuable minerals are collected in a concentrate plant, wherein the mined mineral is grinded in a mill into smaller pieces ($< 100\mu$m). In the next stage, the oversized coarse particles are separated, for example, in hydrocyclons. The oversized coarse particles are usually circulated back to the grinding. In the next stage, chemicals (for example, collectors, activators, lime, and sulphuric acid) are added to the concentrate in the conditioning tank. Thereafter, the concentrate is recovered in the froth flotation.

Froth flotation is a separation process in which the valuable mineral is separated from the unwanted material by means of buoyancy in flotation cell(s); see Figures 2.3 and 2.4. Figure 2.3 shows a standard flotation circuit in which the first two cells are so-called rougher cells and the last three ones scavengers. Usually, in the flotation circuit, there are also cleaner cells, in which the concentrate recovered from all the roughers and scavengers is recovered once more. The gangue (tailings) is normally driven to another

flotation circuit (if there are other valuable minerals which are recovered) or to the tailings pond. In the last stage, the valuable mineral is pumped to a thickener. In the thickening process, water is removed from the concentrate. Finally, the concentrate is exported, for example, to a smelting plant; therein, the gangue and other minerals are separated from the wanted mineral.

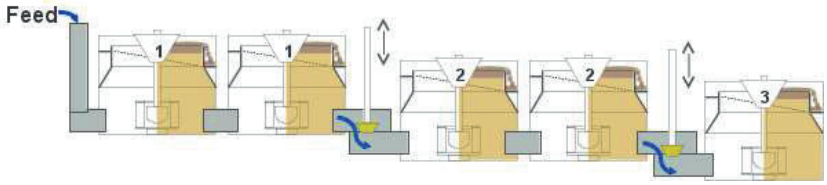

Figure 2.3: An example of a basic flotation circuit (Outotec Oyj, www.outotec.com.).

In the flotation cell, air is dispersed to the bottom of the cell via the rotor shaft; see Figure 2.4. At the bottom of the cell, there is a rotor-stator mechanism which makes the air bubbles smaller when they come out from the center of the rotor. The level of slurry and froth is controlled by the valves of the cell and the aeration rate. The size of the air bubbles and the distribution of air inside the cell have an effect on how the wanted mineral attaches to the surface of the air bubbles [10, 66, 67].

As mentioned earlier, many chemical, operational and mechanical factors have an impact on the efficiency of the flotation process [68–71]. The mechanical factors include, for example, the aeration rate, rotor speed and cell design (the geometries of the flotation cell, stator and rotor). The operational and mechanical factors do not directly affect the metallurgical performance of the flotation cell, but they may create more favorable hydrodynamical conditions.

In the current work, the mixing of air inside a laboratory-size flotation cell was studied (Paper IV). The efficiency of the mixing was studied with ERT, and the so-called gas-holdup distribution inside the laboratory cell was computed and analyzed. Two different rotor-stator mechanisms were analyzed, and their results were compared. Gas holdup distribution is defined as the volume frac-

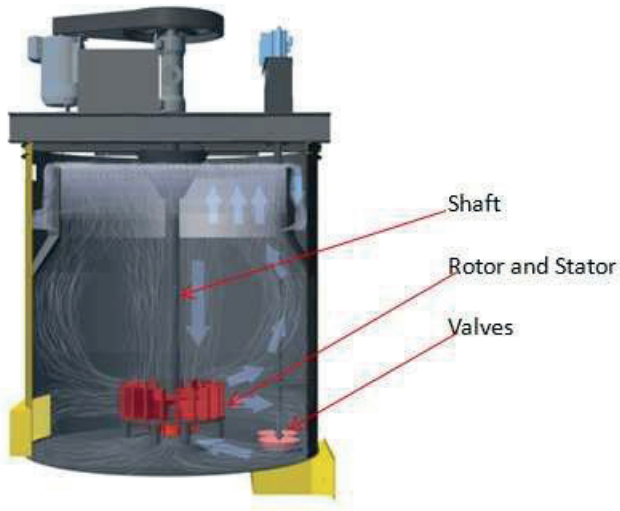

Figure 2.4: A flotation cell design (Outotec Oyj, www.outotec.com).

tion of the gas in the gas-liquid-solid dispersion [72], and it is a very important parameter in characterizing the efficiency of flotation processes and devices [67,73–75].

2.2 RESEARCHING MIXING EFFICIENCY

The quality of mixing significantly affects the end products and also has economic influences on many industrial processes. Therefore, an in-depth understanding of mixing is crucial [1,2]. In order to gain understanding of mixing processes, different types of computational and measurement techniques have been developed.

2.2.1 Mixing index

Mixing efficiency can be characterized in many different ways. One of the most common parameters is the so-called mixing index M_q, which can be defined as

$$M_q = \frac{s}{\bar{q}}, \tag{2.1}$$

where s is the standard deviation of the measured quantity q in the given volume (area), and $\bar{q}$ is the mean value of q. The quantity q can be, for example, conductivity (in the case of ERT), temperature, or the activity of some tracer material, such as a radioactive isotope.

2.2.2 Pulp and paper industry

In pulp and paper production, several methods have been developed to evaluate the performance of mixers [5, 6, 76, 77]. One possibility for the characterization of mixing efficiency is to use inert tracers, such as lithium chloride (LiCl). The tracer is injected to the mixing line; after some delay, samples are collected and analyzed offline [2, 5]. Drawbacks in this type of approach are that online analysis is not possible and that sampling may be problematic and may even disturb the process. Other tracers that can be used to evaluate the quality of mixing are colored dyes and radioactive isotopes [2]. Temperature profiling is a non-invasive method which can also be used to evaluate the quality of mixing [2, 76, 78, 79]. In this method, several temperature sensors are attached to the periphery of, or in some cases also inside, the process pipe. The mixing index of the mixer can be estimated based on the measured temperature profiles. The disadvantage in the temperature profiling method is that the information is acquired (mainly) from the boundary of the pipe; therefore, the mixing efficiency in the whole volume of the process pipe cannot be estimated. Another drawback is that the response time of the temperature sensor is relatively slow, in the range of 0.5-1 s.

2.2.3 Minerals engineering

In froth flotation, the effectivity (or hydrodynamics) of the flotation cell has been studied, for example, with computational fluid dynamics (CFD) [8,9]. The drawback of CFD is that it can only be used offline for studying the behavior of flotation cells; it cannot be used for online process monitoring. Some non-invasive measurement methods, such as Laser Doppler Velocimetry (LDV), Phase-Doppler

Anemometry (PDA), and Particle Image Velocimetry (PIV) have also been used to study the hydrodynamics of flotation cells [9–12]. In addition, CCD camera-based methods have been used in to measure the bubble size in flotation cells [13,14]. Since the camera gives information only on the surface, no mixing information is obtained with camera-based approaches.

There are also several invasive methods for studying the mixing efficiency of flotation cells and columns. Studies on these are based on estimating the gas holdup distribution inside the cells. The most common and promising devices are conductivity probes [67,73,75, 80–86]. The use of such probes for determining the gas holdup is based on Maxwell's relationship between conductivity and the mixture [83,85,87]. The drawback in invasive methods is that only local information near the device is obtained; being invasive, the measurement itself can disturb the process. There are also some studies in which the gas holdup has been analyzed using ERT in bubble column reactors [32,88,89] and in two-phase flows [30,33,90, 91]. However, even today, empirical observations are an important factor in flotation cell design and control.

3 Electrical resistance tomography

In electrical resistance tomography, conductivity distribution $\sigma = \sigma(x, y, z)$ of the object $\Omega \subset \mathbb{R}^3$ is estimated based on the known injected currents I_l and measured voltages U_l on the boundary of the object, on which N_{el} contact electrodes e_l are attached; see Figure 3.1. The measured object is required to have material inside the object which is at least partially conductive.

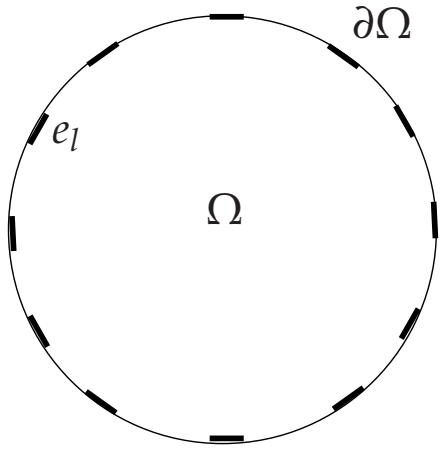

Figure 3.1: Illustration of the ERT measurement, the electrodes e_l are attached to the boundary $\partial\Omega$ of the object Ω.

3.1 ERT MEASUREMENT SYSTEMS

The main parts of an ERT measurement system are shown in Figure 3.2. They include: 1) a control unit, 2) a current injection unit, 3) a voltage measurement unit, and 4) a computer (laptop or PC). The control unit controls the current source(s) and the measurement unit; it communicates with the computer. Usually, the control unit

also computes the demodulation for the measured voltage signal; that is, it calculates the amplitude and phase of the measured voltages. The constant current to the object is created using the current injection unit. The voltages caused by the current injection and the resistivity (conductivity) of the object are measured by the voltage measurement unit. Finally, the image reconstruction is carried out in a computer, which usually contains the graphical user interface (GUI) for controlling the EIT system (measurement protocol) and image reconstruction.

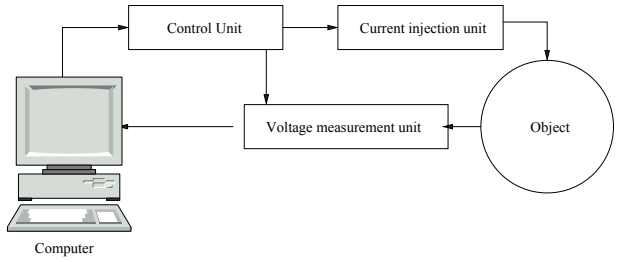

Figure 3.2: Different stages of an ERT measurement system.

3.1.1 Current injection

In ERT, the aim is to inject constant currents to the object, no matter what the conductivity of the object is. Therefore, in ERT, the current injection unit is one of the most important and critical parts of the system, with a considerable impact on the quality of the reconstructed images. Many different types of current sources have been developed for ERT systems. The most common one used in ERT is the Howland-based architecture voltage-to-current converter [92–99].

Another factor that significantly affects the image reconstruction quality is the current injection protocol, that is, how the current is injected into the object with the electrodes. Current injection approaches can roughly be divided into two categories: *pair* and *multiple drive* methods.

In the *pair*, method the current injection is done between two

electrodes, and the most common protocols are the adjacent and opposite current injections. For example, in adjacent protocol in a two-dimensional (2D) system with 16 electrodes, current injections between the electrode pairs $1-2, 2-3, 3-4 \ldots, 15-16, 16-1$ are carried out; for each current injection, voltages from all the 16 electrodes are measured; see Figure 3.1. In this case, one image (or frame) reconstruction uses $16 \times 16 = 256$ voltage measurements. In the opposite current injection protocol with 16 electrodes, current injections between the electrode pairs $1-9, 2-10, 3-11, \ldots, 15-7, 16-8$ are carried out. In this case, voltages are measured from 8 pairs of electrodes. This means that the data used for one image reconstruction consists of $8 \times 16 = 128$ voltage measurements. If the reciprocity principle is taken into account, only 96 measurements in the opposite current injection case are independent. An alternative (interleaved-drive) 2D current pattern has been introduced [100]. Moreover, in 3D imaging, many different *electrode pair*-based current patterns modified from the opposite or adjacent 2D protocols can be used [101].

In the *multiple drive* method, current injection is done simultaneously using multiple electrodes. Thus, better current density than with the *pair* method is achieved inside the object [7]. Usually, the *multiple drive* method is used to optimize the current injection into the object. There are different approaches how the optimal current pattern is achieved. These are, for example, *trigonometric current patterns*, *adaptive current patterns* and statistical inversion-based current patterns [7, 102]. Moreover, the requirements for *multiple drive* current pattern methods are the exact calibration of the current injection channels and the opportunity to make parallel current injections.

3.1.2 Voltage measurement

The voltage measurement in ERT is always made with respect to some reference electrode(s). How this is usually done is based on two approaches: differentially between some electrode pairs, or us-

ing one of the electrodes as a reference in all the measurements [92].

Demodulation

The amplitude and the phase of the measured voltages are obtained using either analogical or digital demodulation. In this section, one digital demodulation technique is briefly explained [103]. The principle of digital demodulation is as follows: the measured signal from the instrumentation amplifier is converted from an analog signal to a digital signal (A/D conversion). In the next step, the sampled signal is directed to the signal processor, which computes the real V_r and the imaginary part V_q of the measured signal as follows:

$$V_\mathrm{r} = \frac{2}{N} \sum_{i=0}^{N-1} V_\mathrm{in}(i) \sin \frac{2\pi i}{N} \tag{3.1}$$

$$V_\mathrm{q} = \frac{2}{N} \sum_{i=0}^{N-1} V_\mathrm{in}(i) \cos \frac{2\pi i}{N} \tag{3.2}$$

where N is the number of the samples and V_in is the input voltage. Amplitude A and phase ϕ of the signal can be computed as follows:

$$A = \frac{2}{N} \sqrt{V_\mathrm{r}^2 + V_\mathrm{q}^2} \tag{3.3}$$

$$\phi = \tan^{-1} \frac{V_\mathrm{q}}{V_\mathrm{r}}. \tag{3.4}$$

In the case of ERT, the V_q is very small, and the phase angle is close to zero; only the voltage amplitude consisting of the real part V_r is used for image reconstruction.

3.1.3 Development of ERT/EIT systems

Nowadays, there are many types of EIT/ERT systems around the world; they are either designed for laboratory use or for industrial and medical applications [51–57, 104–106]. A list of ERT/EIT systems designed for laboratory use can be found in [107]. These include, for example, TIE4, ACT3, MK3 EITS, OXBACT III and KIT2.

In the process and medical industries, there are some companies, e.g., ITS Plc. (www.itoms.com), Outotec (Finland) Oy, (www.outotec.com), Swisstom AG (www.swisstom.com) and Dräger (www.draeger.com), which have their own commercial EIT/ERT systems for different fields in the process and medical industries. Moreover, many research groups around the world have their own EIT/ERT systems designed for specific applications, mainly for medical research [23, 53, 107].

3.2 IMAGE RECONSTRUCTION IN ELECTRICAL RESISTANCE TOMOGRAPHY

In ERT, the conductivity distribution of the object is normally computed through an iterative process in which both the forward and the inverse problem solutions need to be updated. In the forward problem, the voltages on the electrodes are determined when the injected currents and conductivity of the object are known. The *complete electrode model* (CEM) [108–113] is the most accurate and successful forward model in ERT/EIT [114, 115]; it is explained briefly in this section. There are also other models, such as *shunt, gap and continuum models*, which are used in ERT [108, 109, 116].

In the inverse problem of ERT, the conductivity distribution of an object is computed based on the measured voltages and the known injected currents. It is a known fact in ERT that even large changes inside the object may cause only small changes in measured voltages [7]. This feature makes ERT image reconstruction an ill-posed inverse problem, i.e., the problem is unstable, and the solution may be non-unique. To solve the inverse problem of ERT, regularization methods should be used [7, 16, 117–119]. One common regularization method is Tikhonov regularization [16], which allows the use of prior information of the object in the image reconstruction. In this section, a short review on the inverse problem of ERT is provided.

3.2.1 Forward problem

The complete electrode model of the EIT is written as

$$\nabla \cdot \sigma(x)\nabla u(x) = 0, \quad x \in \Omega \tag{3.5}$$

$$u(x) + z_\ell \sigma(x)\frac{\partial u(x)}{\partial n} = U_\ell, \quad x \in e_\ell \subset \partial\Omega, \tag{3.6}$$

$$\int_{e_\ell} \sigma(x)\frac{\partial u(x)}{\partial n} dS = I_\ell, \quad x \in e_\ell \subset \partial\Omega, \tag{3.7}$$

$$\sigma(x)\frac{\partial u(x)}{\partial n} = 0, \quad x \in \partial\Omega \backslash \bigcup_{\ell=1}^{N_{el}} e_\ell, \tag{3.8}$$

where $x \in \mathbb{R}^m$, $m = 2$ or 3 is the position vector, $u(x)$ is the potential distribution inside the domain Ω, z_ℓ is the effective contact impedance between electrode e_ℓ and the object, and n is the outward unit normal vector at $\partial\Omega$. For more information on contact impedance estimation, see [120, 121]. Moreover, the following conditions for the injected currents and measured voltages must be fullfilled

$$\sum_{\ell=1}^{N_{el}} I_\ell = 0, \tag{3.9}$$

$$\sum_{\ell=1}^{N_{el}} U_\ell = 0. \tag{3.10}$$

In this thesis, the finite element method (FEM) is used as a discretization of the forward problem [16, 111, 122].

The weak formulation of the complete electrode model needed in the FEM computations was originally introduced in [109]; it was also reviewed, for example, in [110]. It can be shown that $(u, U) \in H^1(\Omega) \otimes \mathbb{R}^L = H$ is the weak solution of the complete electrode model such that

$$\mathcal{B}((u, U), (v, V)) = \sum_{\ell=1}^{N_{el}} I_\ell V_\ell, \quad \forall \ (v, V) \in H, \tag{3.11}$$

where $\mathcal{B}$ is the bilinear form $\mathcal{B} : H \times H \to \mathbb{R}$

$$\mathcal{B}((u,U),(v,V)) = \int_\Omega \sigma \nabla u \cdot \nabla v \mathrm{d}x + \sum_{\ell=1}^{N_{el}} \frac{1}{z_\ell} \int_\ell (u - U_\ell)(v - V_\ell) \mathrm{d}S. \tag{3.12}$$

The potential distribution $u(\boldsymbol{x})$ is then approximated within the object Ω as

$$u^h(\boldsymbol{x}) = \sum_{i=1}^{N_n} \alpha_i \phi_i(\boldsymbol{x}), \tag{3.13}$$

where N_n is the number of nodes in the finite element mesh, and $\phi_i(x)$ are nodal basis functions of the finite element mesh. Moreover, the voltages U on the electrodes are also approximated as

$$U^h = \sum_{j=1}^{N_{el}-1} \beta_j n_j. \tag{3.14}$$

where vector n_j is chosen such that the condition (3.10) is fulfilled.

Using the theory of finite elements [123], substituting the approximating functions (3.13) and (3.14) in the variational equation (3.11) and choosing $v = \varphi_j, V = n_k$ leads to a matrix equation

$$A\theta = \hat{I}, \tag{3.15}$$

where

$$\theta = \begin{bmatrix} \alpha \\ \beta \end{bmatrix} = \begin{bmatrix} \begin{pmatrix} \alpha_1 \\ \alpha_2 \\ \vdots \\ \alpha_{N_n} \end{pmatrix} \\ \begin{pmatrix} \beta_1 \\ \beta_2 \\ \vdots \\ \beta_{N_{el}-1} \end{pmatrix} \end{bmatrix} \in \mathbb{R}^{N+N_{el}-1} \tag{3.16}$$

is the solution vector and $\hat{I}$ is the data vector, that is,

$$\hat{I} = \begin{bmatrix} \mathbf{0} \\ \sum_{\ell=1}^{N_{el}} I_\ell (n_j)_\ell \end{bmatrix} = \begin{bmatrix} \mathbf{0} \\ \mathcal{C}^T I \end{bmatrix}. \tag{3.17}$$

where the matrix $\mathcal{C} \in \mathbb{R}^{N_{el} \times (N_{el-1})}$ is a sparse matrix having n_j's as columns such that

$$\mathcal{C} = \begin{bmatrix} 1 & 1 & \cdots & 1 \\ -1 & 0 & \cdots & 0 \\ 0 & -1 & & 0 \\ \vdots & & \ddots & \vdots \\ 0 & 0 & \cdots & -1 \end{bmatrix}. \tag{3.18}$$

Moreover, the matrix $A \in \mathbb{R}^{(N+N_{el}-1)\times(N+N_{el}-1)}$ is a sparse block matrix given by

$$\begin{aligned} A(\sigma, z) &= \begin{bmatrix} \mathcal{B}((\varphi_i, 0), (\varphi_k, 0)) & \mathcal{B}((0, n_i), (\varphi_k, 0)) \\ \mathcal{B}((\varphi_i, 0), (0, n_k)) & \mathcal{B}((0, n_i), (0, n_k)) \end{bmatrix} \\ &= \begin{bmatrix} B(\sigma) + C(z) & D(z)\mathcal{C} \\ (D(z)\mathcal{C})^T & \mathcal{C}^T E(z)\mathcal{C} \end{bmatrix}, \end{aligned} \tag{3.19}$$

where the blocks are

$$B_{i,j}(\sigma) = \int_\Omega \sigma \nabla \varphi_i \cdot \nabla \varphi_j \, \mathrm{d}x \, \mathrm{d}y \quad 1 \le i, j \le N \tag{3.20}$$

$$C_{i,j}(z) = \sum_{\ell=1}^{L} \frac{1}{z_\ell} \int_{e_\ell} \varphi_i \varphi_j \, \mathrm{d}S \quad 1 \le i, j \le N \tag{3.21}$$

$$D_{i,j}(z) = -\frac{1}{z_j} \int_{e_j} \varphi_i \, \mathrm{d}S \quad 1 \le i \le N, \quad 1 \le j \le L \tag{3.22}$$

$$\begin{aligned} E_{i,j}(z) &= \sum_{\ell=1}^{L} \frac{1}{z_\ell} \int_{e_\ell} (n_i)_\ell (n_j)_\ell \, \mathrm{d}S \\ &= \begin{cases} 0, & i \neq j \\ \frac{|e_j|}{z_j} & i = j \end{cases} \quad 1 \le i, j \le L \end{aligned} \tag{3.23}$$

where the area of the electrode e_j is $|e_j|$. The potentials $U_\ell^h, \ell = 1, \ldots, L$ on the electrodes are calculated according to equation (3.14)

as

$$\begin{aligned} U_1^h &= \sum_{\ell=1}^{L-1} \beta_\ell \\ U_2^h &= -\beta_1 \\ U_3^h &= -\beta_2 \\ &\vdots \\ U_L^h &= -\beta_{L-1}. \end{aligned} \tag{3.24}$$

These potentials can be represented in the matrix form as

$$U^h = \mathcal{C}\beta, \tag{3.25}$$

The relation between the computed voltages and the injected currents on the electrodes can be expressed thus:

$$U^h = \mathcal{C}\beta = \mathcal{C}\widetilde{\mathcal{R}}^h(\sigma, z)\mathcal{C}^T I = \mathcal{R}^h(\sigma, z)I, \tag{3.26}$$

where $\widetilde{\mathcal{R}}^h(\sigma, z) \in \mathbb{R}^{(L-1)\times(L-1)}$ is a block matrix $(A^{-1})_{i,j}, N+1 \leq i, j \leq N + N_{el} - 1$ of the inverse of the matrix A.

The actual voltage measurements are obtained between the selected electrode pairs, that is, $U_i, i = 1, \ldots, m$, where m is the number of the actual measurements. This can be written in a matrix form as

$$U = MU^h = MR^h(\sigma, z)I = R(\sigma, z)I, \tag{3.27}$$

where $M \in \mathbb{R}^{m\times N_{el}}$ is the measurement matrix.

3.2.2 Inverse problem

The relationship between the conductivity distribution σ, injected currents I and calculated voltages U can be written in the form

$$U(\sigma) = \mathcal{R}(\sigma)I, \tag{3.28}$$

where $\mathcal{R}(\sigma)$ is a so-called *resistivity matrix* [7], which was derived in the previous section; see equation (3.26). Note that therein the

dependence of $R(\sigma, z)$ on z has been left out. The observation model of ERT can be written as

$$V = U(\sigma) + v, \tag{3.29}$$

where noise v of the measured voltages V is assumed to be Gaussian distributed additive noise, $v \sim N(0, \Gamma_v)$.

The inverse problem solution of ERT can be divided into deterministic and statistical inversion approaches. In the next two sections, these inversion approaches are briefly reviewed. For more information, see, e.g., [7, 16, 114].

3.2.3 Deterministic inversion

In deterministic inversion, conductivity distribution σ is considered as an unknown but deterministic variable. The inverse problem is solved by minimizing the weighted least squares functional

$$\|L_v(V - U(\sigma))\|_2^2 \tag{3.30}$$

where L_v is the weighting matrix. Since EIT is a nonlinear *ill-posed* inverse problem, some regularization method is needed. One common regularization method is the generalized Tikhonov regularization [124], which is of the form

$$\hat{\sigma} = \arg\min_{\sigma} \left\{ \|L_v(V - R(\sigma))\|_2^2 + \alpha \|L_\sigma(\sigma - \sigma^*)\|_2^2 \right\} \tag{3.31}$$

where the scalar α is the regularization parameter, L_σ is the regularization matrix in which the prior knowledge of the conductivity distribution is encoded, and σ^* is a predetermined conductivity distribution [22]. The solution of the regularized problem (3.31) can be computed, for example, using an iterative approach. The most common methods when the number of unknowns is small are the Gauss-Newton or Newton-Raphson algorithms [114, 125, 126].

3.2.4 Statistical inversion

In statistical inversion, conductivity distribution σ is assumed to be a random variable; therefore, σ has a probability distribution. In deterministic inversion, σ is assumed to be unknown but non-random.

In statistical inversion, the prior density of σ can be defined as $\pi(\sigma)$ and the posterior probability density of σ given the measured voltages V can be written as

$$\pi(\sigma|V) = \frac{\pi(V|\sigma)\pi(\sigma)}{\pi(V)} \tag{3.32}$$

$$\propto \pi(V|\sigma)\pi(\sigma) \tag{3.33}$$

where the probability density (likelihood density) of measurements V given σ is $\pi(V|\sigma)$, which represents the *forwad model* of ERT [7, 16, 114]. The likelihood density can be written as

$$\pi(V|\sigma) \propto \exp\Big\{ -\frac{1}{2}(V - U(\sigma))^T \Gamma_v^{-1}(V - U(\sigma)) \Big\}. \tag{3.34}$$

The assumptions in (3.34) are that v is Gaussian with zero mean and that σ and v are independent.

Prior information contains all information about the parameter before the measurements. The Gaussian prior density can be written as

$$\pi(\sigma) \propto \exp\Big(-\frac{1}{2}(\sigma - \sigma^*)^T \Gamma_\sigma^{-1}(\sigma - \sigma^*) \Big). \tag{3.35}$$

It can clearly be seen from (3.35) that different prior models can be obtained by changing the covariance matrix Γ_σ. In this thesis, the Gaussian smoothness prior is used; this is the most commonly used prior model, i.e., $\Gamma_\sigma = L_\sigma^T L_\sigma$, where L is a discrete approximation of some differential operator [7]. Other prior models are, for example, anistropic smoothness prior and non-Gaussian priors, such as L^1- and total-variation priors [22, 127–129]. When the prior models are Gaussian distributions, the posterior density of σ can be written as

$$\pi(\sigma|V) \propto \exp\Big(-\frac{1}{2}(V - R(\sigma))^T \Gamma_v^{-1}(V - R(\sigma)) - \frac{1}{2}(\sigma - \sigma_*)^T \Gamma_\sigma^{-1}(\sigma - \sigma_*) \Big). \tag{3.36}$$

The maximum a posterior (MAP) estimate is written as

$$(\sigma)_{MAP} = \arg\max_\sigma \pi(\sigma|V). \tag{3.37}$$

It gives the maximum point of the posterior density and leads to a minimization problem. In the nonlinear case, the MAP estimate can be computed as

$$\sigma_{i+1} = \sigma_i + \kappa_i \left[J_i^T \Gamma_v^{-1} J_i + \Gamma_\sigma^{-1} \right]^{-1} \left[J_i^T \Gamma_v^{-1} (V - U(\sigma_i)) - \Gamma_\sigma^{-1} (\sigma_i - \sigma^*) \right] \tag{3.38}$$

where the Jacobian matrix is

$$J = \frac{\partial U(\sigma)}{\partial \sigma} = \begin{bmatrix} \frac{\partial U^{(1)}}{\partial \sigma_1} & \cdots & \frac{\partial U^{(1)}}{\partial \sigma_M} \\ \vdots & \ddots & \vdots \\ \frac{\partial U^{(K)}}{\partial \sigma_1} & \cdots & \frac{\partial U^{(K)}}{\partial \sigma_M}, \end{bmatrix}$$

where $U^{(k)}$ is the vector $U^{(k)} = R(\sigma) I^{(k)}$, where k refers to the k'th current pattern.

Difference imaging

In many industrial applications, processes are very fast; iterative reconstruction methods may appear to be too slow for practical purposes. Moreover, *absolute imaging* is very sensitive to many errors [19]. One solution to get faster and less error-sensitive image reconstruction is difference imaging.

In difference imaging, the difference of σ between two time instants is estimated. Usually, the 'first' time instant is a reference situation (e.g., a homogenous circumstance) and the 'second' time instant is taken when the conductivity of the object has changed. Formally, voltages V_{ref} at conductivity σ_{ref} are measured as a reference and then compared to voltages V at another time instant with conductivity σ. Finally, the difference $\delta\sigma = \sigma - \sigma_{\text{ref}}$ is estimated. The linearized observation model (3.29) in this case can be written as

$$V \approx V_0 + J_R(\sigma - \sigma_0) + v \tag{3.39}$$

where σ_0 is the linearization point, $V_0 = R(\sigma_0) I$ and $J_R = J_R(\sigma)|_{\sigma=\sigma_0}$. Moreover, (3.39) at the reference situation can be written as

$$V_{\text{ref}} \approx V_0 + J_R(\sigma_{\text{ref}} - \sigma_0) + v_{\text{ref}}, \tag{3.40}$$

where v_{ref} is additive measurement noise in the reference situation. The difference between the reference and the measured voltages is of the form

$$\underbrace{V - V_{\text{ref}}}_{\delta V} \approx J_R \underbrace{(\sigma - \sigma_{\text{ref}})}_{\delta\sigma} + \underbrace{v - v_{\text{ref}}}_{\delta v}. \tag{3.41}$$

The Tikhonov regularized solution can be written in the form

$$\widehat{\delta\sigma} = \arg\min_{\delta\sigma} \{ \|L_{\delta v}(\delta V - J_R \delta\sigma)\|_2^2 + \alpha^2 \|L_{\delta\sigma}\delta\sigma\|_2^2 \} \tag{3.42}$$

and the solution of (3.42) can be written in the form

$$\widehat{\delta\sigma} = (J_R^T \Gamma_{\delta v}^{-1} J_R + \Gamma_{\delta\sigma}^{-1})^{-1} J_R^T \Gamma_{\delta v}^{-1} \delta V. \tag{3.43}$$

The assumption in the difference reconstruction is that the conductivity distribution does not differ much from the reference conductivity. Moreover, if reference conductivity distribution σ_{ref} can be estimated, the equation (3.43) can be written in the form

$$\sigma = \sigma_{\text{ref}} + B\delta V \tag{3.44}$$

where $B = (J_R^T \Gamma_{\delta v}^{-1} J_R + \Gamma_{\delta\sigma}^{-1})^{-1} J_R^T \Gamma_{\delta v}^{-1}$. It should be noted that the matrix B can be computed before any measurements, which makes the difference imaging much faster than absolute imaging. Moreover, systematic errors (for example, calibration errors in injection and/or measurement channels) are avoided with difference imaging.

3.2.5 Approximation error

In publication IV of this thesis, the approximation error approach was used to correct the artefact caused by the unknown liquid level in the flotation cell, [19,130]. In the approximation error approach, the observation model can be written in the form

$$\begin{aligned} V &= U(\sigma, \tilde{k}) + (U^\delta(\bar{\sigma}, k) - U(\sigma, \tilde{k})) + v \\ &= U(\sigma, \tilde{k}) + \epsilon(\bar{\sigma}, k) + v \\ &= U(\sigma, \tilde{k}) + \eta, \end{aligned} \tag{3.45}$$

where $\tilde{k}$ is the approximative nuisance parameter. The relation between σ and $\bar{\sigma}$ is written as $H\bar{\sigma} = \sigma$, where H is an interpolation matrix. In this thesis (Publication IV), k is the height of the liquid in the flotation cell and $\tilde{k}$ is the height of the computation domain in the inverse computations [19]. The approximation error is represented as $\epsilon(\bar{\sigma}, k)$ due to the discretization and approximative parameter $\tilde{k}$. Moreover, we denote $\eta = \epsilon + v$, which is a function of random variables. The equation (3.45) leads to the posterior density of the form

$$\pi(\sigma, V) \propto \exp\Bigg(-\frac{1}{2}(\sigma - \sigma^*)\Gamma_\sigma^{-1}(\sigma - \sigma^*) \\ -\frac{1}{2}(V - U(\sigma, \tilde{k}) - \eta_{*|\sigma})^T\Gamma_{\eta|\sigma}^{-1}(V - U(\sigma, \tilde{k}) - \eta_{*|\sigma})\Bigg), \quad (3.46)$$

where it is assumed that $\Gamma_{\epsilon\sigma} = 0$ and $\Gamma_{v\sigma} = 0$, which means that $\Gamma_{\eta\sigma} = 0$, [19]. With this assumption

$$\eta_{*|\sigma} \approx \epsilon^* + v^* \quad (3.47)$$

$$\Gamma_{\eta|\sigma} \approx \Gamma_\epsilon + \Gamma_v, \quad (3.48)$$

.

It was found that the estimates computed by this method were feasible in several applications; for more information, see [19]. The MAP estimate with the approximation error model is similar to the conventional noise model; see equation (3.31). The minimization problem in this case can be written as

$$\sigma_{\text{MAP}} = \arg\min\left\{\|L_{\eta|\sigma}(V - U^h(\sigma, \tilde{k}) - \eta_{*|\sigma})\|^2 + \|L_\sigma(\sigma - \sigma^*)\|_2^2\right\}, \quad (3.49)$$

where $L_{\eta|\sigma}$ is the Cholesky factor of $\Gamma_{\eta|\sigma}^{-1} = L_{\eta|\sigma}^T L_{\eta|\sigma}$. More about the theory of the approximation error approach can be found in [19].

Computation of approximation error statistics

In this thesis, the statistics of the approximation error is computed using Monte Carlo simulations, in which a set of N_s samples are

generated; these samples are then used for the computation of the accurate and target model solutions $U^{\delta}(\bar{\sigma}^{(i)}, k^{(i)})$ and $U(\bar{\sigma}^{(i)}, \tilde{k})$, where $i = 1, 2 \ldots, N_s$ [19]. The samples $\epsilon^{(i)}$ of the approximation error for the combined unknown nuisance parameter and the discretization errors are obtained as

$$\epsilon^{(i)} = U^{\delta}(\bar{\sigma}^{(i)}, k^{(i)}) - U(H\bar{\sigma}^{(i)}, \tilde{k}). \tag{3.50}$$

Finally, the statisticapproximation error ϵ and the parameter σ are estimated as

$$\xi_* = \frac{1}{N_s} \sum_{i=1}^{N_s} \xi^{(i)}, \Gamma_{\xi} = \frac{1}{N_s - 1} \sum_{i=1}^{N_s} \Psi^{(i)} \Psi^{(i)T}, \tag{3.51}$$

where

$$\xi^{(i)} = \begin{pmatrix} \epsilon^{(i)} \\ \sigma^{(i)} \end{pmatrix}, \Psi^{(i)} = \begin{pmatrix} \epsilon^{(i)} \\ \sigma^{(i)} \end{pmatrix} - \begin{pmatrix} \epsilon_* \\ \sigma_* \end{pmatrix} \tag{3.52}$$

and

$$\Gamma_{\xi} = \begin{pmatrix} \Gamma_{\epsilon} & \Gamma_{\epsilon\sigma} \\ \Gamma_{\sigma\epsilon} & \Gamma_{\sigma} \end{pmatrix} = \begin{pmatrix} \Gamma_{\epsilon} & 0 \\ 0 & \Gamma_{\sigma} \end{pmatrix}. \tag{3.53}$$

4 Review of studies

In this chapter, a review of the results obtained in Publications I-IV is given.

4.1 STUDY I: A PXI PLATFORM BASED ELECTRICAL IMPEDANCE TOMOGRAPHY SYSTEM

In study I, an electrical impedance tomography system was built, mainly from commercially available components. The EIT system was designed such that it was not limited to any predetermined measurement protocol.

The system developed consists of 16 parallel current injection channels and 80 parallel voltage measurement channels; see Figure 4.1. The number of current injection channels is limited to 16 because it has been shown that the number of current injection channels need not to be the same as the number of voltage measurement channels, for example, when using the Kalman filter approach in image reconstruction [131–133].

4.1.1 Materials and methods

In this section, the different stages of the KIT4 (Kuopio Impedance Tomography 4) EIT system are briefly explained. The KIT4 system consists of a PXI and EIT-specific units as shown in Figure 4.2. The PXI is a solid PC-based platform for measurement and automation systems. The PXI combines PCI electrical-bus features with the modular, Eurocard packaging of CompactPCI and then adds specialized synchronization buses and key software features. The PXI platform was developed in 1997 and launched in 1998 by National Instruments (NI). The PXI-based EIT-specific unit was developed and produced in-house in the Department of Applied Physics, University of Kuopio, Finland.

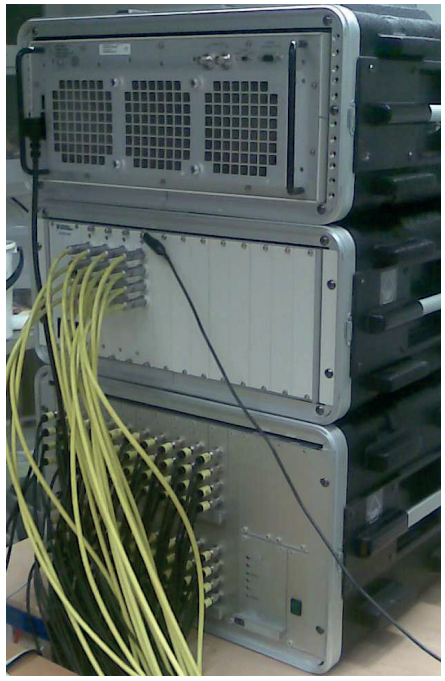

Figure 4.1: The KIT4 system consisting of three different units. The top unit is the controller and analog signal output and input cards. In the middle, there is the current injection unit; at the bottom is the measurement unit.

Current injection unit

In the KIT4 system, the current injection unit consists of two components: a waveform synthesis unit and a voltage-controlled-current source (VCCS) [101,134]. The NI PXI 6713 analog output (AO) card is used to generate an analog waveform (normally a sinusoidal voltage signal) to the VCCS. The range of the voltage signal can be between ± 10 V. The VCCS is based on the current mirror technique and is realized using a commercially available current feedback amplifier (AD844); see Figure 4.3 [135]. This unit also contains analog switches in which the cables of the electrodes can be connected to the current source. The KIT4 system has 16 independent current injection channels.

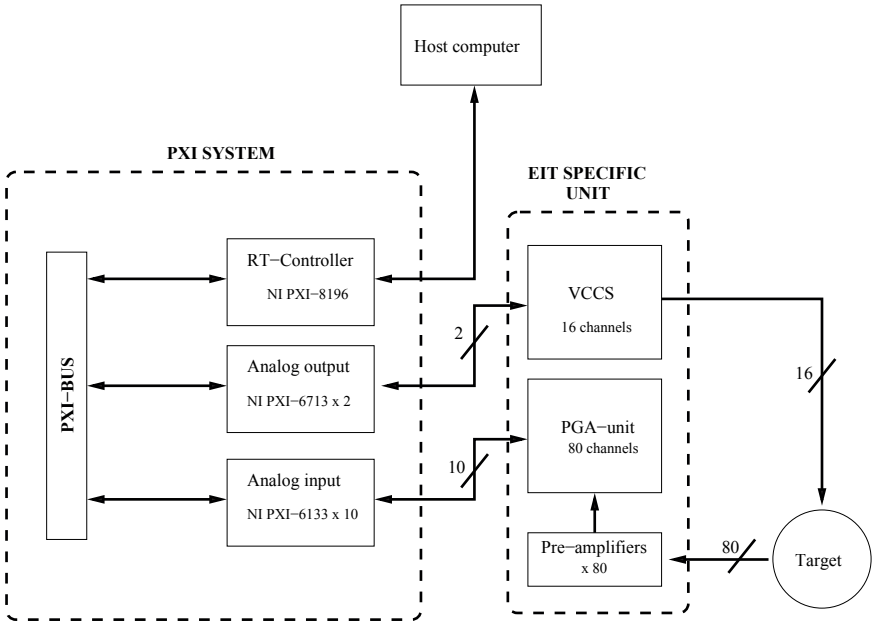

Figure 4.2: Block diagram of the KIT4 system.

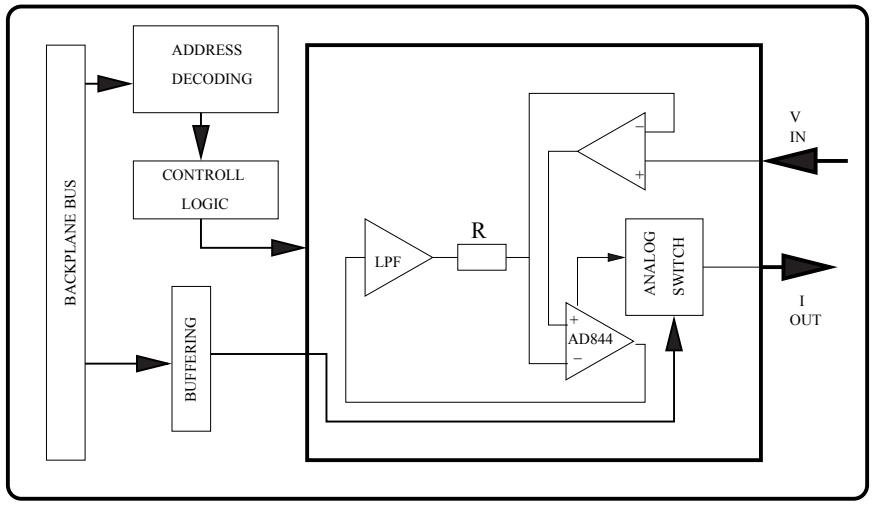

Figure 4.3: Block diagram of the VCCS.

Voltage measurement unit

The voltage measurement unit consists of three different components: two pre-amplifying units and a data acquisition (DAQ) unit. The first pre-amplifier sub-unit (based on the OPA602AU operational amplifier) is attached directly to the electrodes. The main function of the pre-amplifier stage is to minimize the front-end loading of the object. The programmable gain amplifier (PGA) is used in the next stage. The gain of the PGA can be adjusted to be 1, 10 or 100. The third stage in this chain involves the NI PXI-6133 DAQ card, which can acquire data (14 bit resolution) simultaneously from eight channels. There are 10 DAQ cards in the KIT4 system; therefore, up to 80 channels can be measured simultaneously. Digital demodulation of the measured signal is done in the controlling unit.

Controlling unit

The KIT4 system has a NI PXI-8916 realtime (RT) controller, which runs measurement software (made with NI Labview and C/C++ programming languages). The KIT4 system runs in RT mode, and the Phar Lap ETS operating system is used. The controlling of the whole KIT4 system can be done with an additional PC/laptop via Ethernet. Moreover, image reconstruction can be done with the additional PC running Matlab or a C++ based visualization program.

A summary of the details of the KIT4 system is shown in Table 4.1.

4.1.2 Results and discussion

Several performance tests of the KIT4 system were conducted. Noise, stability, linearity response and the speed of the system was evaluated. Moreover, the signal-to-noise ratio (SNR) was calculated as a function of the measurement channel, load and measurement frame rate. In this section, the results of the SNR and the noise tests are

Table 4.1: A summary of the KIT4 system.

Current injection		Voltage measurement	
Number of channels	16 independent ch.	Number of channels	80 independent ch.
Resolution	12 bits	ADC resolution	14 bits
Frequency range	1 kHz - 120 kHz	ADC input voltage range	±1.25 V, ± 2.5 V, ± 5.0 V, ± 10 V
Amplitude range	0 - 5 mA	PGA gain	1,10 or 100
Waveform type	arbitrary	Demodulation	digital
Output impedance	17MΩ @ 15 kHz	Sensitivity	0.15 mV @ PGA gain = 1 @ input voltage ± 1.25V
Target resistance	50Ω-20kΩ		

summarized. The other results can be found in the original publication.

SNR

In this section, SNR measurements as a function of the measurement channel, load and measurement frame rate are briefly reviewed. The SNR for measurement channels was calculated using a circular resistor object, in which 16 precision resistors (resistance 1 ± 0.01 kΩ) were used. The minimum value of the SNR (59.3 dB) was measured on a grounded electrode, due to the low signal level. In the literature, EIT system SNRs vary from 40 dB to 100 dB, depending on many different factors [136,137]. The SNR as a function of the load was measured using a variable resistor; the range of the load was restricted to 50Ω - 20 kΩ. The SNR varied from a minimum of 66.1 dB ($R = 50\Omega$) to 103 dB at ($R = 3.2k\Omega$). The SNR was above 95 dB at $R > 3.2$ kΩ; this is comparable to the results presented in [138].

In SNR as a function of the measurement frame rate, a cylindrical saline phantom was used as an object. 16 electrodes were attached to the boundary of the phantom, and the adjacent current injection method was used. The measurement frame rate was limited to 2 fps - 31.25 fps. The SNR ranged from 58.2 dB at 31.25 fps to

94 dB at 2 fps. The results of this performance test are comparable with those of other EIT systems [136, 138].

Noise

In this section, the results of the noise measurements are briefly reviewed. The same circular resistor object as in the SNR of the measurement channel tests was used. Current injection was switched off and channel one was grounded, avoiding the floating of voltages. The number of samples N_{smp} was 500. The sample mean and standard deviation (std) for each channel were computed. The minimum mean was $\bar{V}_{\mathrm{min}} = 0.08$ mV and $std_{V,\mathrm{min}} = 0.041$ mV on channel one, while the maximum mean was $\bar{V}_{\mathrm{max}} = 0.16$ mV and $std_{V,\mathrm{max}} = 0.093$ mV on the furthermost channel (channel 10).

4.1.3 Summary

Several performance tests were conducted. The results indicate that an efficient PXI-based EIT system can be built up. The performance of this system is at least same as that of other EIT systems [107].

4.2 STUDY II: IMAGING OF MIXING OF THE TWO MISCIBLE LIQUIDS USING ELECTRICAL IMPEDANCE TOMOGRAPHY

In study II, the mixing of two miscible liquids in a turbulent flow is studied using two different chemical injection methods: the Trumpjet® mixing system and a conventional nozzle injection. This work was presented in Publication II.

4.2.1 Materials and methods

The measurements were carried out in a mixing loop in the Savonlinna Fiberlaboratory at Lappeenranta University of Technology. The mixing loop consisted of a 17 m^3 water tank and a recirculation pipe (DN400) loop. The KIT4 measurement system and a linear impedance sensor (for details, refer to original publication) were used in the measurements; see Figure 4.4. In this section, the results of the linear impedance sensor are not shown; the results can be found in the original publication. The positions of the KIT4 electrodes in the first and second measurement cases and the position of the linear impedance sensor can be viewed in Figure 4.4.

In the first measurement set-up (3D ERT), there were 64 electrodes in four layers. The number of electrodes in one electrode layer was 16. The first layer was 138 mm above the Trumpjet mixing system. Five experiments were carried out, in which the conventional chemical injection was compared to different Trumpjet injections (four experiments); see table 4.2. Both the Trumpjet injection rate and the injection speed of the tracer were changed.

In the second measurement case, there were 32 ERT electrodes in one layer, 1700 mm above the Trumpjet system. The linear impedance sensor was installed 2300 mm above the Trumpjet system. Three experiments were conducted (based on customer choice): Experiments 1, 2 and 4; see table 4.2.

In both cases, the velocity of the main flow was 3 m/s, and 0.4% saline was used as a tracer. The exact values of the injection rate and the speed of the chemical are not given as they are technical

trade secrets. Therefore, the values are marked as X in table 4.2. The image reconstruction approach used is presented in Chapter 3.

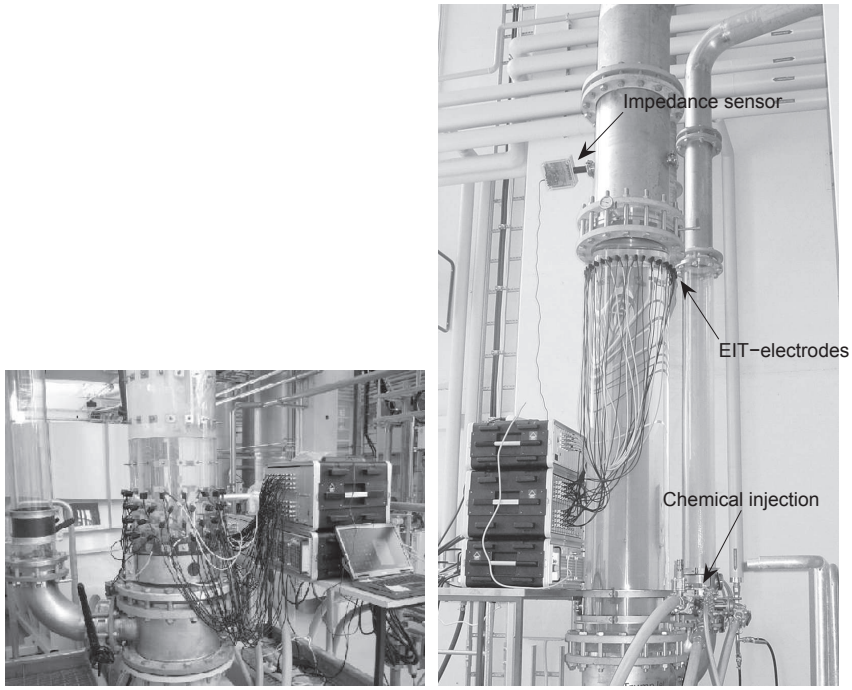

Figure 4.4: Left: The first measurement set-up. Right: The second measurement set-up.

Table 4.2: Test experiments in measurement cases 1 and 2. See the text for the clarification of the experiments.

		Injection rate of the chemical (l/s)	Injection speed of the chemical
Experiment 1	Conventional Injection	X	X
Experiment 2	Trumpjet Injection	40 times X	18 times X
Experiment 3	Trumpjet Injection	60 times X	28 times X
Experiment 4	Trumpjet Injection	80 times X	37 times X
Experiment 5	Trumpjet Injection	100 times X	47 times X

4.2.2 Results and discussion

Case 1

The average of the 500 conductivity images was computed, and relative deviation $RD(h)$ at different height levels h was computed as

$$RD(h) = \frac{std(\sigma;h)}{mean(\sigma;h)}, h = 1,\ldots,40(\text{cm}), \tag{4.1}$$

where $std(\sigma;h)$ is the cross-sectional standard deviation of the averaged conductivity distribution at height h. The $mean(\sigma;h)$ is the cross-sectional average of the averaged conductivity distribution at height h. The results in the first measurement case in different experiments are shown in Figure 4.5. A clear difference can be ob-

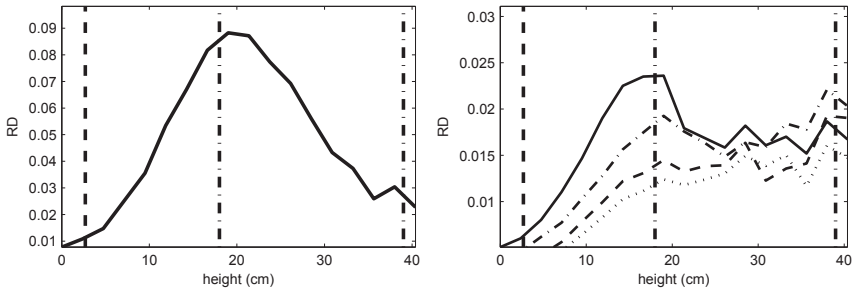

Figure 4.5: RD in different experiments as a function of height, left: Experiment 1, right: Experiment 2 (solid line), Experiment 3 (dash-dotted line), Experiment 4 (dashed line) and Experiment 5 (dotted). The dotted vertical line denotes the position of the chemical injection. The two vertical dash-dotted lines denote the location of the first and fourth electrode layers.

served between the conventional and the Trumpjet injections. The maximum value of the RD in the conventional injection (Experiment 1) is almost 0.085 while in Experiments 2-5 the maximum value is below 0.025; this means that the mixing is more effective when Trumpjet is used. Moreover, in Experiments 2-5, the RD starts to decrease faster than in Experiment 1; this validates that mixing is more effective with the Trumpjet injection than with the conventional one. It can also be seen in the results that the injection rate affects the efficiency of the mixing. In other words, in Experiment

5 (with the biggest injection rate), the maximum of the *RD* is the smallest, and the *RD* starts to decrease faster than in the other experiments.

Case 2

The 2D ERT images of the second measurement set-up are shown in Figure 4.6. There is a clear difference between the conventional and the Trumpjet injections. In the conventional injection, the mixed chemical (tracer) flows near the wall of the pipe whereas in the Trumpjet experiment, the mixed chemical is spread out more over the whole intersection of the pipe.

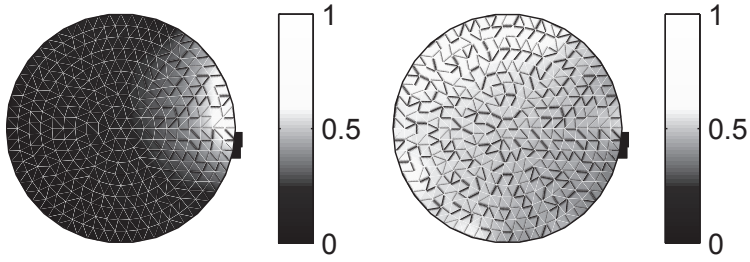

Figure 4.6: Normalized conductivity distributions. Left: Classical chemical injection (Experiment I), Right: Trumpjet chemical injection. The black dots denote the position of the chemical injection point.

4.2.3 Summary

Using ERT, this study has demonstrated that with the conventional injection, the mixing of the chemicals to the main flow is not so effective as with Trumpjet®. The injection rate of the chemical has an effect on the mixing efficiency. Furthermore, ERT with saline as a tracer can be used to study mixing efficiency.

4.3 STUDY III: MEDIUM CONSISTENCY MIXER PERFORMANCE IMAGING USING ELECTRICAL RESISTANCE TOMOGRAPHY

In study III, the evaluation of a medium-consistency mixer was performed. The measurements were carried out using the KIT4 EIT system; as a reference method, a multipoint temperature sensor was used. This work was presented in Publication III.

4.3.1 Materials and methods

Measurements in this study were carried out in a medium consistency loop (MC-loop) at the Savonlinna FiberLaboratory pilot plant of the Lappeenranta University of Technology. The MC-loop consisted of a pumping system with MC-technology with a flow rate corresponding to a production rate of 100-5000 admt/d[1], a reaction vessel and a thickener for consistency control. The mixer used was an AMix AC30-25. The rotation speed of the mixer varied between 900-1500 rpm.

The KIT4 system was used for ERT measurements, with 48 stainless steel electrodes attached around the process pipe (electrodes on three layers, diameter of the pipe 300 mm). ERT sensors were placed at a distance of 1820 mm from the mixer; see Figures 4.7 and 4.8. The image reconstruction approach used is presented in Chapter 3. There were eight temperature sensors around the pipe (thermocouples, type NiCr/Ni, response time 0.3 s) at a distance of 750 mm from the mixer.

Four different measurement cases were studied with bleached soft-wood ($T = 70°C$). The pulp flow was 150 l/s at 10% consistency. Cold water ($T = 10°C$, injection rate =15 l/s), air (room temperature) and steam ($T = 150°C$) were used as tracers. Here, three measurement cases (1,2 and 3) are briefly explained; see the list below. The results of the fourth case can be found from in Publication III.

[1] admt/d = air dried metric tonne per day

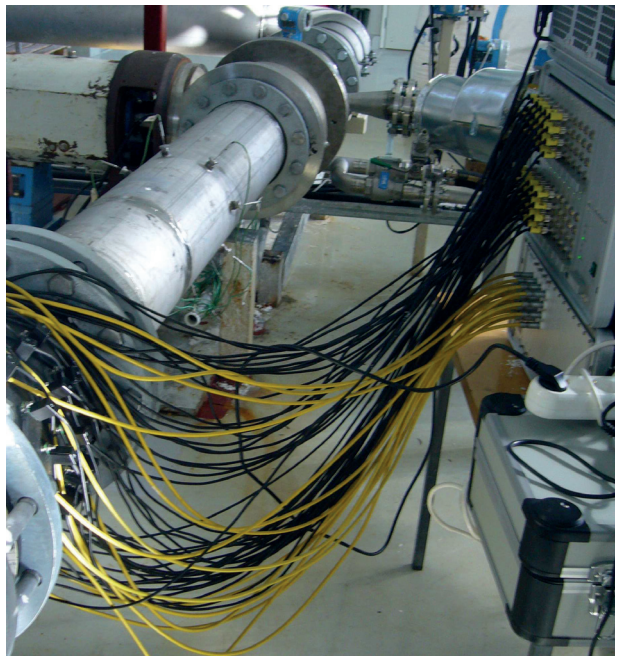

Figure 4.7: The measurement set-up.

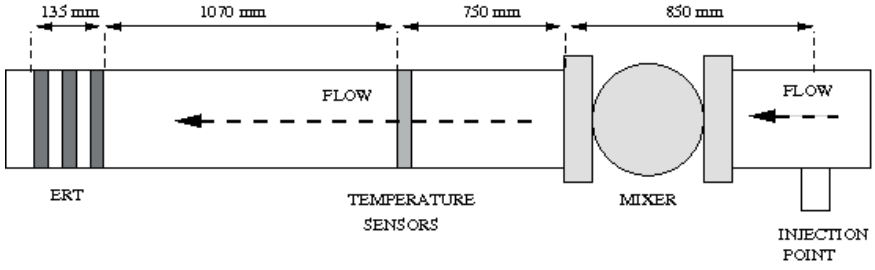

Figure 4.8: A schematic drawing of the measurement setup.

- Case 1: Cold water OFF (A), cold water ON (B), mixer ON (C), mixer OFF and cold water OFF (D).
- Case 2: Air OFF (A), air ON (2 l/s) (B), mixer ON (C), mixer OFF (D), air OFF (E).
- Case 3: Air OFF (A), air ON (5 l/s), mixer ON (C), mixer OFF (D), air OFF (E).

The time spans of the different process stages, such as ”cold water on (B)”, are shown in the following figure in gray/white color 4.9.

4.3.2 Results and discussion

The results of the first set-up are shown in Figures 4.9 and 4.10. The normalized temperatures under temperature sensors 1, 3, 5, 7 and the conductivity values under electrodes 2, 6, 10 and 14, both as a function of time, are shown in Figure 4.9.

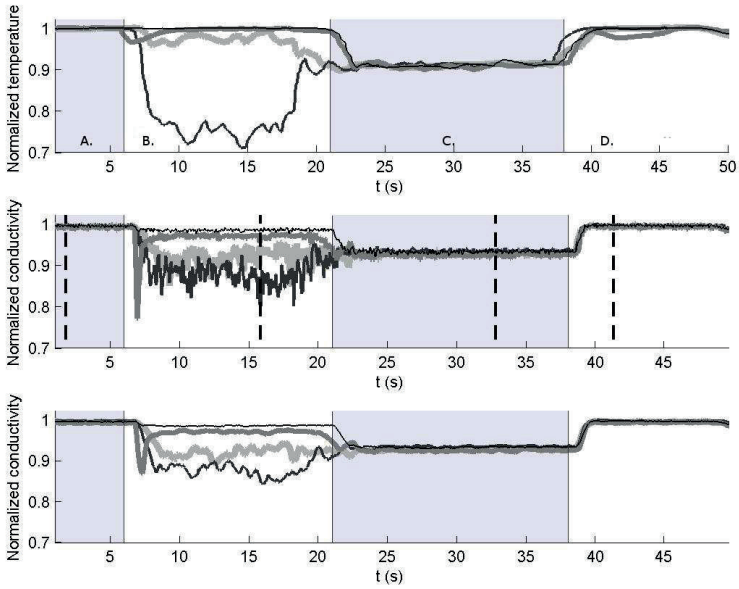

Figure 4.9: Results from Case 1. Upper graph: Normalized temperature profiles of sensors 1 (thick light gray), 3 (thick black), 5 (thick dark gray) and 7 (thin black) as a function of time. Middle graph: Normalized conductivity values under ERT electrodes 2,6,19 and 14 as a function of time. Vertical dashed lines denote the times at which the snapshots were taken for Figure 4.10. Lower graph: Filtered (windowed average) of the ERT data. The numbered areas A, B, C and D in the upper graph denote the time spans of different process stages.

It is clear that both measurement methods could detect the cold water injection and the effect of the mixer. The temperature dropped

during stage B; in the same stage, the conductivity measured by ERT decreased to a maximum of 0.15 units. The conductivity of cold water was lower than that of process water. When the mixer is set to ON (stage C), both temperature and conductivity values stabilize. Moreover, differences between channels decrease; which means that the cold water is mixed with the main flow. When the mixer is set to OFF (stage D), both methods detect the stage change. The variation in the ERT measurements is higher than that in the temperature sensors; this indicates that that of the response time of the ERT is much higher than the temperature sensors.

In Figure 4.10, the cross-sectional slices at four different points of time are shown. The advantage of ERT compared to the temperature sensor can be seen from these snapshots. The location of the water in the process pipe prior to mixing can clearly be seen; see Figure 4.10 b. Moreover, the effect of mixing is also clearly visible, i.e., how homogenously cold water is distributed to the whole volume when the mixing is set to on; see Figure 4.10 c.

In Cases 2 and 3, air was used as a tracer. The results are shown in Figure 4.11. In these two cases, temperature sensors were not able to measure differences inside the pipe; the temperature drop caused by the air was too small. It is evident that the effect of injected air can be detected using ERT. When air injection is set to ON/OFF, there is a big decrease/increase in the conductivity in both cases. Moreover, the effect of the mixer is clear in the conductivity values. In non-filtered conductivity, signal artifacts on the conductivity values can be seen, especially in Case 3 (air flow 5 l/s); this is due to the agglomeration of the air bubbles immediately after the mixer.

4.3.3 Summary

Even though temperature sensors and ERT give similar values, it has been shown that ERT has some advantages over temperature sensors.

1. ERT can give information about mixing in the whole 3D vol-

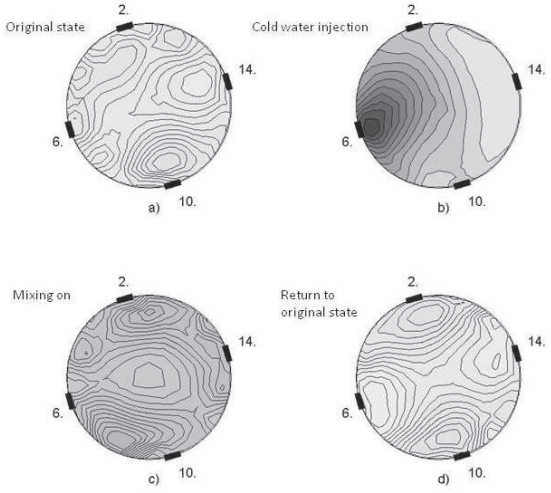

Figure 4.10: Cross-sectional images of the conductivity distribution at four different time instants (see Figure 4.9) in measurement Case 1.

ume inside the measurement section.

2. The response time of ERT is much faster than that of in temperature sensors.

3. ERT detects conductivity changes while a temperature sensor detects only temperature changes. This means that ERT has more detectable factors (e.g. gas, steam, different conductive tracers) than temperature sensors do.

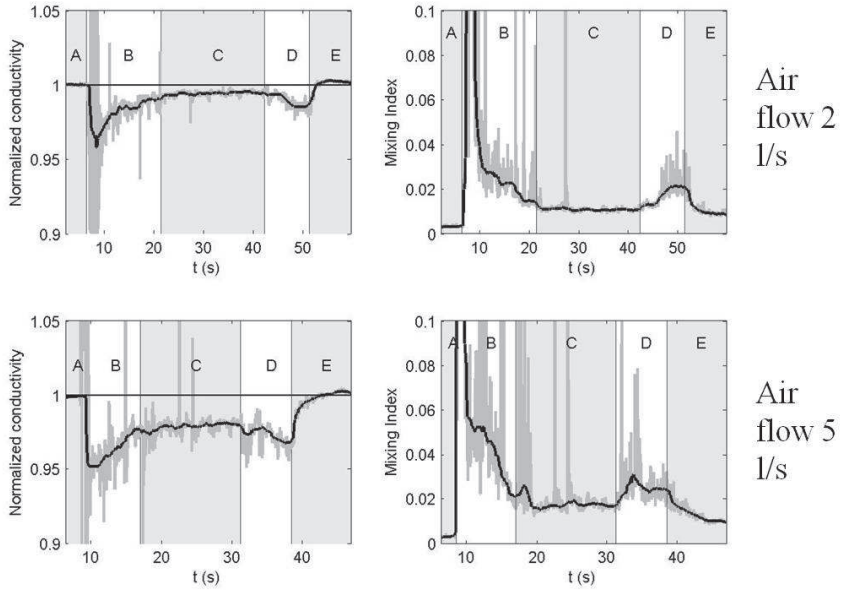

Figure 4.11: Left: Normalized mean conductivities in Cases 2 and 3 as a function of time. Right: Mixing index in Cases 2 and 3. Upper Figure: air injection 2 l/s and Lower Figure: air injection 5 l/s. The areas labelled A, B, C, D and E denote the time spans of different process stages. The grey lines are from the raw conductivity data, and the black lines show a stage after filtering.

4.4 STUDY IV: GAS HOLDUP MEASUREMENTS IN PILOT SCALE FLOTATION CELL USING ELECTRICAL RESISTANCE TOMOGRAPHY

In study IV, the spatial distribution of the gas holdup in a mechanical flotation cell was determined using the KIT 4 EIT system. The gas holdup distribution is presented at various values of the rotor speed and gas superficial velocity in non-frothed and frothed cases. In this study, two rotor-stator mechanisms were compared.

4.4.1 Materials and methods

The experiments were carried out in a cylindrical froth flotation cell (50 dm^3) made of transparent plastic; see Figure 4.12. The

radius and height of the cell were 200 mm and 600 mm, respectively. Two different rotor-stator mechanisms were used (OK-125 and FloatForce®, Outotec Oyj, Finland); see Figure 4.12 and Table 4.3. In the ERT measurements, the KIT4 system with 80 measurement electrodes on the boundary of the cell in 5 layers was used.

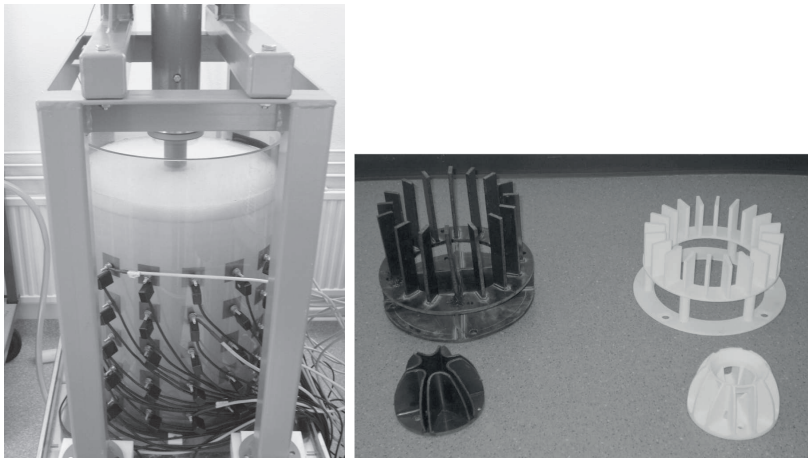

Figure 4.12: Left: The froth flotation cell used in the study. Right: The rotor-stator mechanisms used in the study, (left) OK-125 and (right) FloatForce®.

Table 4.3: The dimensions of rotor-stator mechanisms

	$\text{Stator}_{\text{OK}-125}$	$\text{Rotor}_{\text{OK}-125}$	$\text{Stator}_{\text{FloatForce}}$	$\text{Rotor}_{\text{FloatForce}}$
Diameter (mm)	250	125	220	130
Height (mm)	180	75	120	75

Three experiments were carried out in a two-phase mixture with and without a frother, with two rotor-stator mechanisms. Frother (Dowfroth 250), dosage 15 ppm, and tap water were used. The water level inside the cell was 460 mm in order to prevent overflowing during the test, i.e., the volume of the water was 57 dm^3. In this section, measurement Cases I and III are briefly reviewed. The results of measurement Case II can be found in the original publication.

In measurement Case I, the transient behavior of gas holdup distribution was studied. In the first experiment, rotor velocity was

held constant ($v = 3.39$ m/s, 498 rpm). The superficial gas velocity was

$$J_g = \frac{Q}{A}, \tag{4.2}$$

where Q is the gas flowrate, and A is the cross-sectional area of the cell. The superficial gas velocity was changed from 0 to 0.67 cm/s and divided into six different time intervals. In the second experiment, J_g was held constant, and the velocity of the rotor was changed from 1.36 m/s to 4.07 m/s and divided into five different time intervals. In both cases, an OK-125 rotor-stator mechanism was used without a frother. In Case III, a comparison of the two different rotor-stator mechanisms was made, i.e., the effect of the different mechanisms on the gas holdup distribution was studied. The velocity of the rotors was changed from $\approx$ 200 rpm to $\approx$ 600 rpm, in 100 rpm steps.

4.4.2 Results and discussion

The results of Case I are shown in Figures 4.13 and 4.14. It is evident that J_g has a crucial effect on the gas holdup. At a low superficial gas velocity, there is only a small portion at the bottom of the cell with the gas holdup larger than 3%. When the superficial gas velocity is increased, the global gas holdup is also increased significantly. The cross-sectional averages of the gas holdup on three horizontal layers as a function of time are shown in Figure 4.14. It can be observed that the effect of v on the gas holdup is bigger than the effect of J_g. The gas holdup with higher v values increases at the bottom of the cell significantly, which means that gas dispersion is more effective at higher rotor velocities. This is due to the fact that air bubbles move with the liquid flow rather than rise toward the surface of the mixture. Near the rotor, the movement of the bubbles is more vertical; this is due to lower peripheral speed near the rotor than near the wall. The results of measurement Case III are shown in Figure 4.15. The comparison of the two different rotor-stator mechanisms was studied. It can be seen that there are big differences in the gas holdup, depending on which mechanism is used.

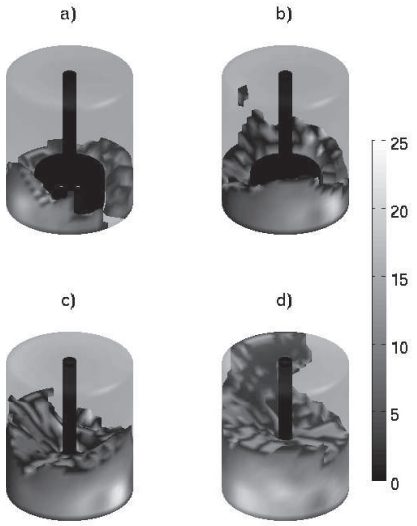

Figure 4.13: Three-dimensional gas holdup distributions at different gas superficial velocities; gas holdup greater than 3% is visualized, rotor radial velocity $v = 3.39$ m/s: (a) $J_g = 0.2$ cm/s, (b) $J_g = 0.33$ cm/s, (c) $J_g = 0.53$ cm/s and (d) $J_g = 0.67$ cm/s.

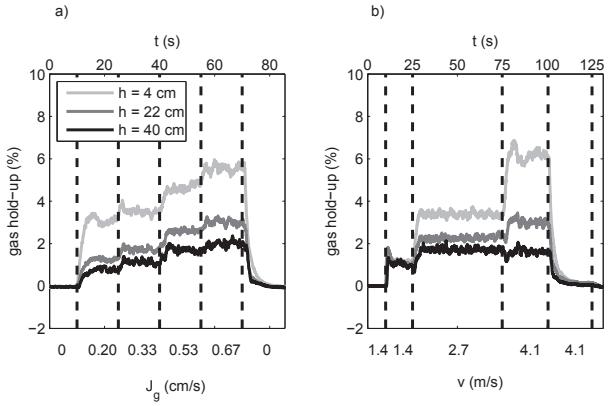

Figure 4.14: The cross-sectional averages of the gas holdup as a function of time: (a) at four J_g cm/s and one $v = 3.39$ m/s, (b) at three v and one $J_g = 0.53$ cm/s.

The maximum gas holdup with the OK-125 mechanism is near the wall at a height of 12 cm, while with FloatForce, the maximum gas holdup is at the bottom of the cell. Moreover, with FloatForce, the

gas holdup distribution in the whole cell is smoother than with the OK-125 mechanism.

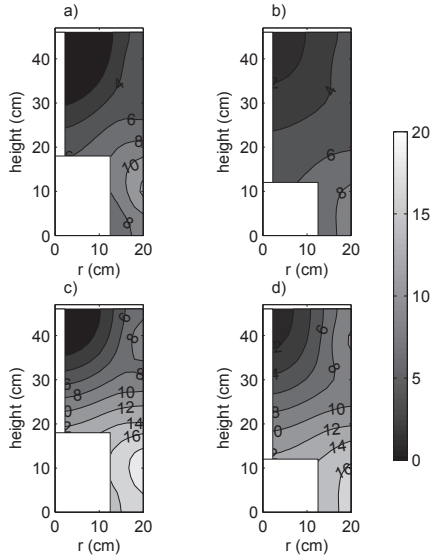

Figure 4.15: Contours of the gas holdup distribution in the vertical plane: (a) OK-125, $v = 2.63$ m/s (b) FloatForce, $v = 2.63$ m/s, (c) OK-125, $v = 3.9$ m/s, (d) FloatForce, $v = 4.1$ m/s

4.4.3 Summary

It was found that ERT can be used to characterize gas holdup in the flotation process under different process conditions. As the rotor velocity increases, the gas holdup also increases, especially at the bottom of the cell. It was also shown that by increasing superficial gas velocity, global gas holdup increases; the measurement system described by Gorain et al. [81] yielded similar results.

The differences in the gas holdup distribution obtained with the two mechanisms are clearly visible. In the case of the OK-125 mechanism, the maximum of the gas holdup was at a height of 12 cm whereas with the FloatForce ® mechanism, it was at the bottom of the cell. Moreover, the gas holdup distribution was more even in the case of the FloatForce ® mechanism.

5 Summary and conclusions

This thesis introduces an ERT system (KIT4) made mainly from commercial components. The performance of the KIT4 system was tested with many generally used testing protocols. The performance of the KIT4 system is also presented in Publications II, III and IV. In those studies, ERT was used to evaluate the performance of mixing and froth flotation common processes in the pulp and paper and mineral industries. In the following subsections, the conclusions of each study are briefly presented.

Publication I

In this study, a PXI-based ERT system (KIT4) was presented. Many components of the KIT4 system are commercially available and suitable for industrial use. However, the most critical parts, the current source and pre-amplifier units, are in-house products. Furthermore, the software for controlling the system and for the visualization were also developed in-house. The temporal resolution of the KIT4 system is quite high. Examination of the effects of fast flows online in 3D is therefore possible. It has been shown based on the laboratory experiments that it is possible to use ERT in mixing and flotation studies.

Publication II

In this study, the mixing performance of two different chemical injection systems was examined. As measurement modalities, ERT and a linear impedance sensor were used. Two different experiments were conducted. In the first one, experiments with five different chemical injection rates were conducted with 3D ERT. In the second experiment, the linear impedance sensor and the ERT were tested. It can be concluded that the differences between the conventional and the TrumpJet chemical injections can be studied using

ERT and the linear impedance sensor.

Publication III

This study has shown that ERT is a suitable measurement technique in medium consistency (MC) mixing studies in the pulp and paper industry. It is also shown that ERT results are similar to those of the well-known temperature profiling. However, the ERT approach was demonstrated to provide more insight into the mixing process by producing real-time 3D images inside the bleaching process.

The volumetric information given by ERT would be a very useful tool when developing mixers and pumps. ERT itself can be useful for finding optimal driving parameters for the pumps the mixer or both, in different pulp and paper processes.

Air detection inside the process pipe is also one important factor; it too can be detected with ERT. Any air entering the process can be very harmful to the pumps (cavitation) and pipes (high pressure). These findings, obtained in a pilot plant having dimensions and flows similar to those in industry, and the ease of application of the method, suggest that ERT can be readily implemented in the real pulp and paper industry to study the bleaching process and the behavior of mixers.

Publication IV

The main purpose of this study was to use 3D ERT for gas holdup estimation in a flotation process. In this work, the measurements were carried out in a two-phase situation using water and air. Moreover, a comparison of the gas holdup distribution between two rotor-stator mechanisms was performed. Several tests with several rotor radial velocities, gas superficial velocities and with and without frother were performed.

It should be noted that gas dispersion inside the laboratory cell is different from that in industrial scale flotation cells. Use of ERT in industrial flotation cells is therefore not so straightforward because

process conditions change continuously. Moreover, the small distance between the rotor and the wall of the cell in the experiments could be problematic. The results of this paper are not necessarily true for a large-size industrial cell.

This study has, however, shown that ERT can be a useful tool when developing new monitoring devices for flotation processes in the mining industry. Moreover, for finding optimal driving parameters (though in laboratory scale) for flotation cells, ERT can be useful because many parameters of flotation cells are scalable to real flotation processes.

In the future, it would be interesting to make a comparison between CFD and ERT results. Also, more measurements in two- and three-phase situations (true froth flotation process) should be performed.

Following this study, ERT technology has been successfully used in three-phase situations for froth flotation by Numcore Oy and Outotec Oyj., proving that ERT technology can be useful indeed in the mining industry.

5.1 CONCLUSIONS

This thesis, has shown that 2D/3D ERT can be used successfully in chosen mixing and froth flotation processes when evaluating the performance of the processes studied. An ERT system can be built up mainly from commercial components, although there are many ready-made commercial ERT systems available. The advantage of an in-house system compared to commercial ERT systems is that the latter are usually developed for some specific applications. In other words, the configuration of a commercial system to suit an application other than the one for which it is designed can be very hard.

Good mixing is very important in many industrial processes. However, there is still a lack of online tools with which the efficiency of mixing in an industrial environment can be detected reliably. Therefore, there is an urgent need in the process industry

for new online measurement methods. Examples of existing ones are tomographic methods, such as ERT, ECT, and ultrasound tomography (UT); and magnetic induction tomography (MIT). Also, the comparison and combination of ERT with so-called hard-field tomography methods (for example, X-ray Tomography (XT), Magnetic Resonance Imaging (MRI) and Positron Emission Tomography (PET)) would generate new knowledge and possibilities when investigating different industrial applications.

Process optimization is nowadays a very important factor, and the need for cost savings has grown rapidly in every industrial field. Other reasons for process optimization include environmental issues. In other words, with optimized processes, it is also possible to save natural resources and decrease chemical, energy, and pure water, consumption. This can be achieved only with well-planned and monitored processes. Therefore, the development of tomographic methods to improve existing industrial processes is justified.

Bibliography

[1] A. Plaskowski, M. S. Beck, R. Thorn, and T. Dyakowski, *Imaging industrial flows: Applications of electrical process tomography* (Taylor & Francis, New York, 1995).

[2] E. L. Paul, V. A. Atierno-Obeng, and S. M. Kresta, *Handbook of Industrial Mixing-Science and Practise* (A John Wiley & Sons, New Jersey, 2003).

[3] C. W. Dence and D. W. Reeve, *Pulp Bleaching: Principles and Practice*, Vol. 24, (TAPPI Press, 1996).

[4] T. York, "Status of electrical tomography in industrial applications," *J. Electron. Imaging.* **10,** 608–619 (2001).

[5] C. P. J. Bennington, C. M. Peters, and R. MacLaren, "Characterization of mixing quality in laboratory pulp mixers," *J. Pulp and Paper* **28,** 459–465 (1997).

[6] C. P. J. Bennington, H. T. Yang, and G. L. Pageau, "Mill assessment of mixing quality using laboratory bleaching studies," *Pulp Paper Can* **102,** 23–27 (2001).

[7] L. M. Heikkinen, *Statistical estimation methods for electrical process tomography*, PhD thesis (University of Kuopio, Finland, 2005).

[8] M. Craddock and J. Swanepol, "Design And Operation Of A New Flotation Cell: Ultimate Flotation.," in *Conference Proceedigs: Flotation Cell Technology Conference* (2007).

[9] P. T. L. Koh, M. P. Schwarz, Y. Zhu, P. Bourke, R. Peaker, and J. P. Frandizidis, "Development of CFD models of mineral flotation cells.," in *Proceedings 3rd International Conference on CFD in the Minerals and Process Industries* (CSIRO, Melbourne, Australia, 2003).

[10] T. Miettinen, M. Laakkonen, and J. Aittamaa, "The applicability of various flow visualization techniques for the characterization of gas-liquid flow in mixed tanks," in *AIChE Annual Meeting* (2002).

[11] J. Tiitinen, J. Vaarno, and S. Gronstrand, "Numerical modelling of an Outokumpu flotation device," in *Proceedings 3rd International Conference on CFD in the Minerals and Process Industries* (CSIRO, Melbourne, Australia, 2003).

[12] A. P. Van der Westhuizen and D. A. Deglon, "Evaluation of solids suspension in a pilot-scale mechanical flotation cell: the critical impeller speed," *Minerals Engineering* **20,** 233–240 (2007).

[13] R. A. Grau and K. Heiskanen, "Visual technique for measuring bubble size in flotation machines," *Minerals Engineering* **15,** 507–513 (2002).

[14] R. A. Grau and K. Heiskanen, "Gas dispersion measurements in a flotation cell," *Minerals Engineering* **16,** 1081–1089 (2003).

[15] J. G. Webster, *Electrical Impedance Tomography* (Adam Hilger, Bristol, UK, 1990).

[16] M. Vauhkonen, *Electrical impedance tomography and prior information*, PhD thesis (University of Kuopio, Finland, 1997).

[17] T. Dyakowski, L. F. C. Jeanmeure, and A. J. Jaworski, "Applications of electrical tomography for gas-solids and liquid-solids flows - a review," *Powder Technol.* **112,** 174–192 (2000).

[18] B. H. Brown, "Electrical impedance tomography (EIT): a review," *J. Med. Eng. Technol.* **27,** 97–108 (2003).

[19] A. Nissinen, *Modelling errors in electrical impedance tomgraphy*, PhD thesis (University of Eastern Finland, Finland, 2011).

[20] F. Santosa and M. Vogelius, "A backprojection algorithm for electrical impedance imaging," *SIAM J Appl Math* **50,** 216–243 (1990).

[21] M. Wang, "Inverse solutions for electrical impedance tomography based on conjugate gradients methods," *Meas Sci Tech* **13,** 101–117 (2002).

[22] J. P. Kaipio and E. Somersalo, *Computational and Statistical Methods for Inverse Problems* (Applied Mathematical Sciences 160, Springer-Verlag, 2005).

[23] R. Mann, W. Wang, A. E. Forrest, P. J. Holden, F. J. Dicking, T. Dyakowski, and R. B. Edwards, "Gas-liquid and miscible liquid mixing in a plant-scale vessel monitored using electrical resistance tomography," *Chem. Eng. Commun.* 39–48 (1999).

[24] S. Kim, N. A. Nkaya, and T. Dyakowski, "Measurement of mixing of two miscible liquids in a stirred vessel with electrical resistance tomography," *Int. Commun. Heat Mass Transfer* **33,** 1088–95 (2006).

[25] W. Yenjaichon, G. Pageau, M. Bhole, C. P. J. Bennington, and J. R. Grace, "Assessment of mixing quality for an industrial pulp mixer using electrical resistance tomography," *The Canadian Journal of Chemical Engineering* **89,** 996–1004 (2011).

[26] B. H. Brown, D. C. Barber, and A. D. Seagar, "Applied potential tomography: possible clinical applications," *Clin. Phys. Physiol. Meas* **6,** 109–121 (1985).

[27] F. J. McArdle, B. H. Brown, R. G. Pearse, and D. C. Barber, "The effect of the skull of low–birthweight neonates on applied potential tomography imaging of centralised resistivity changes," *Clin. Phys. Physiol. Meas, Suppl A* **9,** 55–69 (1988).

[28] D. Murphy, P. Burton, R. Coombs, L. Tarassenko, and P. Rolfe, "Impedance imaging in the newborn," *Clin. Phys. Physiol. Meas, Suppl A* **8,** 131–140 (1987).

[29] V. Rimpiläinen, *Electrical tomography imaging in pharmaceutical processes*, PhD thesis (University of Eastern Finland, Finland, 2012).

[30] Y. Ma, Z. Zheng, L. Xu, X. Liu, and Y. Wu, "Application of electrical resistance tomography system to monitor gas/liquid two-phase flow in a horizontal pipe," *Flow Measurement and Instrumentation* **12,** 259–265 (2001).

[31] R. Mann, F. J. Dicking, M. Wang, T. Dyakowski, R. A. Williams, R. B. Edwards, A. E. Forrest, and P. J. Holden, "Application of electrical resistance tomography to interrogate mixing process at plant scale," *Chem. Eng. Science* **52,** 2087–2097 (1997).

[32] H. Jin, W. Wang, and R. Williams, "Analysis of bubble behaviour in bubble columns using electrical resistance tomography," *Chemical Engineering Journal* **130,** 179–185 (2007).

[33] G. P. Lucas, J. Cory, R. Waterfall, W. W. Loh, and F. J. Dickin, "Measurement of the solids volume fraction and velocity distributions in solids-liquid flows using dual-plane electrical resistance tomography," *Flow Measurement and Instrumentation* **10,** 249–258 (1999).

[34] F. J. Dickin, R. A. Williams, and M. S. Beck, "Determination of composition and motion of multicomponent mixtures in process vessels using electrical impedance tomography–I. Principles and process engineering applications," *Chem. Eng. Sci.* **48,** 1883–97 (1993).

[35] R. M. West, X. Jia, and R. A. Williams, "Quantification of solid-liquid mixing using electrical resistance and positron emission tomography," *Chem. Eng. Comm.* **175,** 71–97 (1999).

[36] M. Wang and J. J. Cilliers, "Detecting non-uniform foam density using electrical resistance tomography," *Chemical Engineering Science* **54,** 707–712 (1999).

[37] M. Wang, A. Dorward, D. Vlaev, and R. Mann, "Measurements of gas-liquid mixing in a stirred vessel using electrical resistance tomography," *Chem. Eng. J.* **77,** 93–8 (2000).

[38] M. S. Beck and R. Williams, *Process Tomography: Principles, Techniques and Applications* (Butterworth-Heinemann, 1995).

[39] P. J. Holden, M. Wang, R. Mann, F. J. Dickin, and J. B. Edwards, "Imaging stirred-vessel macromixing using electrical resistance tomography," *AIChE journal* **44,** 780–790 (1998).

[40] F. Gumery, F. Ein-Mozaffari, and Y. Dahman, "Macromixing hydrodynamic study in draft-tube airlift reactors using electrical resistance tomography," *Bioprocess Biosyst. Eng.* **34,** 135–144 (2011).

[41] L. Pakzad, F. Ein-Mozzaffari, and P. Chan, "Using electrical resistance tomography and computational fluid dynamics modeling to study the formation of cavern in the mixing of pseudoplastic fluids possessing yield stress," *Chemical Engineering Science* **63,** 2508–2522 (2008).

[42] M. Sharifi and B. Young, "3-Dimensional spatial monitoring of tanks for the milk processing industry using electrical resistance tomography," *Journal of Food Engineering* **105,** 312–319 (2011).

[43] T. L. Rodgers, D. R. Stephenson, M. Cooke, T. A. York, and R. Mann, "Tomographic imaging during semi-batch reactive precipitation of barium sulphate in a stirred vessel," *Chemical Engineering Research and Design* **87,** 615–626 (2009).

[44] D. R. Stephenson, T. L. Rodgers, R. Mann, and T. A. York, "Application of three dimensional electrical impedance tomography to investigate fluid mixing in a stirred vessel," in *Proc. 13th European Conference on Mixing* (2009).

[45] J. Kourunen, A. Rinne, K. Saloheimo, T. Niitti, and L. M. Heikkinen, "Electrical tomography imaging of flotation pro-

cess in a mechanical flotation cell," in *5th International Symposium of Process Tomography in Poland* (2008).

[46] J. J. Cilliers, W. Xie, S. J. Neethling, E. W. Randall, and A. J. Wilkinson, "Electrical resistance tomography using bi-directional current pulse technique," *Measurement Science and Technology* **12,** 997–1001 (2001).

[47] P. Paananen, J. Matula, J. Kourunen, and J. Heikkinen L. M, Käyhkö, "Evaluating mixing efficiency when paper chemicals are fed close to the headbox," in *Proceedings of Papermaking Research Symposium* (2009).

[48] M. R. Bhole and C. P. J. Bennington, "Performance of four axial flow impellers for agitation of pulp suspensios in a laboratory-scale cylindrical stock chest," *Ind. Eng. Chem. Res.* **49,** 4444–4451 (2010).

[49] Y. Rubin and S. Hubbard, *Hydrogeophysics* (Springer, Netherlands, 2005).

[50] A. Lehikoinen, *Modeling Uncertainties in Process Tomography and Hydrogeophysics*, PhD thesis (University of Eastern Finland, Finland, 2012).

[51] T. I. Oh and D. Woo, E. J. Holder, "Multifrequency EIT system with radially symmetric architechture: KHU Mark1," *Physiol. Meas.* **29,** 183–96 (2007).

[52] A. J. Wilkinson, E. W. Randall, L. T. M., and A. Collins, "The design of an ERT system for 3D data aqcuistion and quantitative evaluation of its performance," *Meas. Sci. Technol.* **17,** 2088–2096 (2006).

[53] A. J. Wilson, P. Milnes, A. R. Waterworth, R. H. Smallwood, and B. H. Brown, "Mk3.5: a modular, multi-frequency successor to the Mk3a EIS/EIT system," *Physiol. Meas.* **22,** 49–54 (2001).

[54] M. Wang, Y. Ma, N. Holliday, Y. Dai, R. A. Williams, and G. Lucas, "A high performance EIT system," *IEEE Sensor J.* **15,** 289–99 (2005).

[55] R. D. Cook, G. J. Saulnier, D. G. Gisser, J. C. Goble, N. J. C., and D. Iisaacson, "ACT3: a high speed high precission electrical impedance tomograph," *IEEE Trans. Biomed. Eng* **41,** 713–722 (1994).

[56] R. Halter, A. Hartov, and K. Paulson, "Design and implementation of a high frequency electrical impedance tomography system," *Physiol. Meas.* **25,** 379–390 (2004).

[57] G. J. Saulnier, N. Liu, C. Tamma, H. Xia, T.-J. Kao, J. C. Newell, and D. Isaacson, "An electrical impedance spectroscopy system for breast cancer detection," in *Proc. 20th Annual Int Conf* (IEEE EMBS, Lyon, France, 2007), pp. 4154–7.

[58] D. C. Barber and B. H. Brown, "Applied potential tomography," *J. Phys.E: Sci. Instrum.* **17,** 723–33 (1984).

[59] T. Savolainen, J. P. Kaipio, M. Vauhkonen, and P. A. Karjalainen, "An EIT measurement system for experimental use," *Rev. Sci. Instrum.* **67,** 3605–9 (1996).

[60] G. Xu, R. Wang, S. Zhang, S. Yang, G. A. Justin, M. Sun, and W. Yan, "A 128-electrode three dimensional electrical impedance tomography system," in *Proc. 20th Annual Int Conf* (IEEE EMBS, Lyon, France, 2007), pp. 4386–9.

[61] R. Deloughry, I. Ibrahim, P. V. S. Ponnapali, P. Lingard, and D. Benchebra, "PXI-based electrical capacitance tomography imaging system applied t flow control and mass flow measurement," in *Proceedings of the 5th World Congress on Industrial Process Tomography* (2007).

[62] M. Santori, "An instrument that isn't really," *IEEE Spectr.* **27,** 36–9 (1990).

[63] J.-M. Teini, "Täyteaineen retentio ja paperitekninen potentiaali," (2011), Barchelor Thesis, Tampere University of Applied Sciences, Finland, In Finnish.

[64] J. Matula, "Immediate and efficient mixing of wet end additives close to PM headbox," http://www.wetend.com (Accessed: 2013-06-14).

[65] J. Matula, "Advanced use of filler close to headbox together with retention aid additives with Trumpjet® Flash Mixing system," http://www.wetend.com (Accessed: 2013-06-14).

[66] M. C. Fuerstenau, G. Jameson, and R.-H. Yoon, *Froth Flotation: A Century of Innovation* (Society for Mining, Metallurgy, and Exploration, 2007).

[67] E. Sanwani, Y. Zhu, J.-P. Franzidis, E. V. Manlabig, and J. Wu, "Comparison of gas holdup distribution measurement in a flotation cell using capturing and conductivity techniques," *Minerals Engineering* **19,** 1362–1372 (2006).

[68] J. A. Finch, J. Xiao, C. Hardie, and C. Gomez, "Gas disperision properties: bubble surface area flux and gas holdup," *Minerals Engineering* **13,** 365–372 (2000).

[69] D. A. Deglon, D. Egya-Mensah, and J. P. Franzidis, "Review of hydrodynamics and gas dispersion in flotation cells on South African platinum concentrators," *Minerals Engineering* **13,** 235–244 (2000).

[70] P. T. L. Koh and M. P. Schwarz, "CFD modelling of bubble-particle attachments in flotation cells," *Minerals Engineering* **19,** 619–626 (2006).

[71] J. Turunen, A. Rinne, S. Grönstad, T. Niitti, and K. Schommarz, "How to transfer installed power efficiently into flotation performance," in *Proceedings: Flotation Cell Technology Conference* (2007).

[72] J. B. Joshi, U. Parasu Veera, C. V. Prasad, D. V. Phanikumar, N. S. Deshphande, S. S. Thakre, and B. N. Thorat, "Gas Holdup Structure in Bubble Column Reactors–Review Article," *PINSA* **64,** 441–567 (1998).

[73] C. O. Gomez, F. Cortez-Lopez, and J. A. Finch, "Industrial testing of gas holdup sensor for flotation systems," *Minerals Engineering* **16,** 493–501 (2003).

[74] J. Tabera, "Local gas holdup measurement in stirred fermenters. I. Description of the measurement apparatus and screening of variables," *Biotechnology Techniques* **4,** 299–304 (1990).

[75] F. J. Tavera, R. Escudero, and J. A. Finch, "Gas holdup in flotation columns: laboratory measurements," *International Journal of Mineral Processing* **61,** 23–40 (2001).

[76] W. B. Rewatkar, R. J. Kerekes, and C. P. J. Bennington, "Use of temperature profiling to measure mixing quality in pulp bleaching operations," *Pulp Paper Can* **103,** 21–27 (2002).

[77] N. Kamal and C. P. J. Bennington, "An On-line, In-Situ, Mixing Assesment Technique for Pulp Fibre Suspensions," *J. Pulp Paper Sci* **26,** 214–220 (2000).

[78] L. O. Torregrossa, "Effect of mixing efficiency on Chloride Dioxide bleaching," in *TAPPI Pulping Conference* (1983).

[79] D. Peschell, "Goulds introduces New Techology in Mixing," *PumpLines summer* **4** (2001).

[80] B. K. Gorain, J. P. Franzidis, and E. V. Manlapig, "Studies of impeller type, impeller speed and air flow rate in industrial scale flotation cell. Part 1: Effect on bubble size distribution," *Minerals Engineering* **8,** 615–635 (1995).

[81] B. K. Gorain, J. P. Franzidis, and E. V. Manlapig, "Studies of impeller type, impeller speed and air flow rate in indus-

trial scale flotation cell. Part 2:Effect on gas holdup," *Minerals Engineering* **8,** 1557–1570 (1995).

[82] R. Pérez-Garibay and R. del Villar, "On-line gas holdup measurement in flotation columns," *Canadian Metallurgical Quarterly* **38,** 141–148 (1999).

[83] A. M. Arizmendi-Morquecho, R. Pérez-Garibay, A. Uribe-Salas, and F. Nava-Alonso, "On-line solids holdup measurement in mineral slurries by the standard addition method," *Minerals Engineering* **15,** 61–64 (2002).

[84] S. Schwarz, "Gas dispersion measurements in industrial flotation cells," *Minerals Engineering* **19,** 554–560 (2006).

[85] C. O. Gomez and J. A. Finch, "Gas dispersion measurements in flotation cells," *International Journal of Mineral Processing* **84,** 51–58 (2007).

[86] J. Yianatos, F. Contreras, and F. Díaz, "Gas holdup and RTD measurement in an industrial flotation cell," *Minerals Engineering* **23,** 125–130 (2010).

[87] J. C. Maxwell, *A Treatise of Electricity and Magnetism. vol 1.* (Oxford University press, third ed., London, 1892).

[88] M. Fransolet, P. Crine, P. Marchot, and D. Toye, "Analysis of gas holdup in bubble columns with non-Newtonian fluid using electrical resistance tomography and dynamic gas disengagement technique," *Chemical Engineering Science* **60,** 6118–6123 (2005).

[89] R. A. Williams, "Minerals and material processing," Chap 11 in *Process Imaging for Automatic Control*, D. M. Scott and H. McCann, eds. (Taylor & Francis, USA, 2005).

[90] D. L. George, J. R. Torczynski, K. A. Shollenberger, T. J. O'Hern, and S. L. Ceccio, "Validation of electrical-impedance tomography for measurements of material distribution in two-phase

flows," *International Journal of Multiphase Flow* **26,** 549–581 (2000).

[91] F. Wang, Q. Marashdeh, L.-S. Fan, and R. A. Williams, "Electrical capacitance, electrical resistance and positron emission tomography techniques and their applications in multi-phase flow systems," *Chapter 5, Advances in Chemical Engineering* **37,** 179–222 (2009).

[92] T. Savolainen, *Modulaarinen, adaptiivinen impedanssitomografialaitteisto (in Finnish)*, PhD thesis (University of Kuopio, Finland, 2008).

[93] M. Wang, *Electrical impedance tomography on conducting walled process vesseles*, PhD thesis (UMIST, University of Manchester Institute of Science and Technology, UK, 1994).

[94] A. S. Ross, G. J. Saulnier, J. C. Newell, and D. Isaacson, "Current source design for electrical impedance tomography," *Physiol. Meas.* **24** (2003).

[95] P. Rangraz, A. Sheikhani, and N. Hemmati, "Design and simulation of a current source for electrical impedance tomography," in *IASTED International Multi-Conference Biomedical Engineering* (2006), pp. 396–400.

[96] D. J. Nowicki and J. G. Webster, "A one op-amp current source for electrical impedance tomography," in *Proceedings of 11th Annual International Conference of the IEEE EMBS* (1989), pp. 457–458.

[97] Y. Peng and Y. L. Mo, "A electrical impedance tomography system," in *Proceedings of 25th Annual International Conference of the IEEE EMBS* (2003), pp. 280–281.

[98] Z. Shuai, X. Guizhi, W. Huanli, G. Duyan, and Y. Weili, "Multi-frequency EIT hardware system based on DSP," in *Suppl. of 27th Annual International Conference of the IEEE EMBS* (2006).

[99] C.-Y. Chen, L. Y.-Y., W.-L. Huang, and K.-S. Cheng, "The simulation of current generator design for multi-frequency electrical impedance tomograph," in *Proceedings of the 28th Annual International Conference of the IEEE EMBS* (2006), pp. 6072–6075.

[100] B. M. Eyüboğlu, "An interleaved drive electrical impedance tomography image reconstruction algorithm," *Physiol. Meas.* **17,** 59–71 (1996).

[101] L. M. Heikkinen, J. Kourunen, T. Savolainen, P. J. Vauhkonen, J. P. Kaipio, and M. Vauhkonen, "Real time three-dimensional electrical impedance tomography applied to multiphase flow imaging," *Meas. Sci. Tech.* **17,** 2083–2087 (2006).

[102] J. P. Kaipio, A. Seppänen, E. Somersalo, and H. Haario, "Posterior covariance related optimal current patterns in electrical impedance tomography," *Inv. Probl.* **20,** 919–936 (2004).

[103] R. D. Cook, *ACT3: A high-speed, high-precision electrical impedance tomograph*, PhD thesis (Rensselaer Polytechnic Institute, Troy, New York, 1992).

[104] T. A. York, S. Murphy, A. Burnett-Thompson, and B. Grieve, "An accessible electrical impedance imaging system," in *Proceedings 4th World Congress on Industrial Process Tomography* (2005).

[105] C. Cruickshank, M. Tirkkonen, T. Soini, and J. Kourunen, "Progress in flotation cell level control and determ ination of froth bed thickness using Outotec LevelSense® technology," in *In proceedings of Flotation 13* (2013).

[106] B. D. Grieve, S. Murphy, A. Burnett-Thompson, and T. A. York, "An accessible electrical impedance tomograph for 3D imaging," *Trans. of the Inst. of Meas. and Cont.* **32,** 31–50 (2010).

[107] J. Bourne and editor, *Critical Reviews in Biomedical Engineering* (Begel House Inc., 1996).

[108] K.-S. Cheng, D. Isaacson, N. J. C., and D. G. Gisser, "Electrode models for electric current computed tomography," *IEEE Transactions on Biomedical Engineering* **36,** 918–924 (1989).

[109] E. Somersalo, M. A. Cheney, and D. Isaacson, "Existence and uniqueness for electrode models for electric current computed tomography," *SIAM J Appl Math* **52,** 1023–1040 (1992).

[110] P. J. Vauhkonen, *Image Reconstruction in Three Dimensional Electrical Impedance Tomography*, PhD thesis (University of Kuopio, Finland, 2004).

[111] P. J. Vauhkonen, M. Vauhkonen, T. Savolainen, and J. P. Kaipio, "Three-dimensional electrical impedance tomography based on the complete electrode model," *IEEE Transactions on Biomedical Engineering* **46,** 1150–1160 (1999).

[112] L. Borcea, "Electrical impedance tomography," *Inverse Problems* **18,** R99–R136 (2002).

[113] W. R. B. Lionheart, "EIT Reconstruction Algorithms: Pitfalls, Challenges, and Recent Developments," *Physiol. Meas.* **25,** 125–142 (2004).

[114] A. Seppänen, *State Estimation in Process Tomography*, PhD thesis (University of Kuopio, Finland, 2005).

[115] O.-P. Tossavainen, *Shape Estimation in Electrical Impedance Tomography*, PhD thesis (University of Kuopio, Finland, 2007).

[116] M. Cheney, D. Isaacson, and J. C. Newell, "Electrical impedance tomography," *SIAM Rev* **41,** 85–101 (1999).

[117] J. Sylvester and G. Uhlmann, "A global uniqueness theorem for an inverse boundary value problem," *Ann. of Math.* **125,** 153–169 (1987).

[118] A. I. Nachman, "Global uniqueness for a two-dimensional inverse boundary value problem," *Ann. of Math.* **143,** 71–96 (1996).

[119] K. Astala and L. Päivärinta, "Caldernś inverse conductivity problem in the plane," *Ann. of Math.* **163,** 265–299 (2006).

[120] T. Vilhunen, J. P. Kaipio, P. J. Vauhkonen, T. Savolainen, and M. Vauhkonen, "Simultaneous reconstruction of electrode contact impedances and internal electrical properties: I theory," *Measurement Science and Technology* **13,** 1848–1854 (2002).

[121] L. M. Heikkinen, T. Vilhunen, R. M. West, M. Vauhkonen, and J. P. Kaipio, "Simultaneous reconstruction of electrode contact impedances and internal electrical properties: II. Laboratory experiments," *Meas. Sci. Tech.* **13,** 1855–61 (2002).

[122] N. Polydorides and W. Lionheart, "A Matlab toolkit for three dimensional electrical impedance tomography: a contribution to the electrical impedance and diffuse optical recontruction software project," *Measurement Science and Technology* **13,** 1871–1883 (2002).

[123] S. C. Brenner and L. R. Scott, *The Mathematical Theory of Finite Element Methods* (Springer, 1994).

[124] M. Vauhkonen, D. Vadász, P. A. Karjalainen, E. Somersalo, and J. P. Kaipio, "Tikhonov regularization and prior information in electrical impedance tomography," *IEEE Trans. Med. Imaging* **17,** 285–293 (1998).

[125] P. Hua, J. G. Webster, and W. J. Tompkins, "A regularised electrical impedance tomography reconstruction algorithm," *Clin Phys Meas, Suppl A* **9,** 137–141 (1988).

[126] P. Hua, E. J. Woo, J. G. Webster, and W. J. Tompkins, "Iterative reconstruction methods using regularization and optimal current patterns in electrical impedance tomography," *IEEE Trans Med Imaging* **10,** 621–628 (1991).

[127] J. P. Kaipio, V. Kolehmainen, E. Somersalo, and M. Vauhkonen, "Statistical inversion and Monte Carlo sampling meth-

ods in electrical impedance tomography," *Inv. Probl.* **16,** 1487–1522 (2000).

[128] T. Martin and J. Idier, "A FEM based nonlinear MAP estimator in electrical impedance tomography," in *Proceedings IEEE ICIP97* (1997).

[129] M. Yu and D. E. Dougherty, "Modified total variation methods for three-dimensional electrical resistance tomography inverse problems," *Water Resources Research* **36,** 1653–1664 (2000).

[130] A. Nissinen, L. M. Heikkinen, and J. P. Kaipio, "The bayesian approximation error approach for electrical impedance tomography," *Measurement Science and Technology* **19,** 015501 doi:10.1088/0957–0233/19/1/015501 (2008).

[131] V. Kolehmainen, A. Voutilainen, and J. P. Kaipio, "Estimation of non-stationary region boundaries in EIT-state estimation approach," *Inverse Problems* **17,** 1937–56 (2001).

[132] A. Seppänen, L. Heikkinen, A. Savolainen, T. Voutilainen, E. Somersalo, and J. P. Kaipio, "An experimental evaluation of state estimation with fluid dynamical models in process tomography," *Chem. Eng. J.* **127,** 23–30 (2007).

[133] A. Seppänen, A. Peltola, L. Heikkinen, J. Kourunen, and J. P. Kaipio, "State estimation in process tomography–experimental study in 3D multi-phase flow case," in *Proc. 5th World Congress on Industrial Process Tomography* (2007).

[134] T. Savolainen, L. M. Heikkinen, M. Vauhkonen, and J. P. Kaipio, "A modular, adaptive electrical impedance tomography system," in *Proc. 3rd World Congress on Industrial Process Tomography* (2003), pp. 50–5.

[135] R. Bragos, J. Rosell, and P. Riu, "A wide-band AC-coupled current source for electrical impedance tomography," *Physiol. Meas.* **15,** 91–9 (1994).

[136] A. McEvan, G. Cusick, and D. Holder, "A review of errors in multi-frequency EIT instrumentation," *Physiol. Meas* **28,** 197–215 (2007).

[137] K. S. Cheng, S. J. Simske, D. Isaacson, J. C. Newell, and D. G. Gisser, "Errors due to the measuring voltage on current-carrying electrodes in electric current computed tomography," *IEEE Trans. Biomed. Eng.* **37,** 60–5 (1990).

[138] D. R. Stephenson, T. A. York, and R. Mann, "Performance and requirements of process ERT instruments," in *Proceedings of the 5th World Congress on Industrial Process Tomography* (2007).

Jari Kourunen

Imaging of Mixing in Selected Industrial Processes Using Electrical Resistance Tomography

Today's process industry faces many challenges. Examples are environmental acts and increased expectations of economical profits. For the process industry, these mean increased process efficiency for improved sustainability and competitiveness, leading to process optimization, continuous process monitoring and control of processes. Information on industrial processes is usually based on offline laboratory tests, in situ measurements, or computational fluid dynamics (CFD). In this thesis, the feasibility of three-dimensional electrical resistance tomography (ERT) for monitoring certain selected mixing processes in the pulp and paper and mineral industries is studied. The results show that the chosen mixing processes can be studied successfully with the ERT system developed.

UNIVERSITY OF
EASTERN FINLAND

Publications of the University of Eastern Finland
Dissertations in Forestry and Natural Sciences

ISBN 978-952-61-1637-2